

# Winter Arctic Sea Ice Thickness From ICESat-2 Freeboards

Alek A. Petty<sup>1,2</sup> , Nathan T. Kurtz<sup>1</sup>, Ron Kwok<sup>3</sup> , Thorsten Markus<sup>1</sup> , and Thomas A. Neumann<sup>1</sup>

<sup>1</sup>Cryospheric Sciences Laboratory, NASA Goddard Space Flight Center, Greenbelt, MD, USA, <sup>2</sup>Earth System Science Interdisciplinary Center, University of Maryland, College Park, MD, USA, <sup>3</sup>Jet Propulsion Laboratory, California Institute of Technology, Pasadena, CA, USA

## Key Points:

- We present new estimates of sea ice thickness derived from ICESat-2 freeboards for the first Arctic winter season of data collection
- We highlight the regional and seasonal variability in the Arctic winter sea ice freeboard, snow depth, and thickness distributions
- Our IS-2 thickness estimates are consistently thinner than those estimated from CryoSat-2 data using the same input assumptions

## Supporting Information:

- Supporting Information S1

## Correspondence to:

A. A. Petty,  
alek.a.petty@nasa.gov

## Citation:

Petty, A. A., Kurtz, N. T., Kwok, R., Markus, T., & Neumann, T. A. (2020). Winter Arctic sea ice thickness from ICESat-2 freeboards. *Journal of Geophysical Research: Oceans*, 125, e2019JC015764. <https://doi.org/10.1029/2019JC015764>

Received 10 OCT 2019

Accepted 4 APR 2020

Accepted article online 15 APR 2020

**Abstract** National Aeronautics and Space Administration's (NASA's) Ice, Cloud, and land Elevation Satellite-2 (ICESat-2) mission was launched in September 2018 with the primary goal of monitoring our rapidly changing polar regions. The sole instrument onboard, the Advanced Topographic Laser Altimeter System, is now providing routine, very high-resolution, surface elevation data across the globe, including the Arctic and Southern oceans. In this study, we demonstrate our new processing chain for converting the along-track ICESat-2 sea ice freeboard product (ATL10) into sea ice thickness, focusing our initial efforts on the Arctic Ocean. For this conversion, we primarily make use of snow depth and density data from the NASA Eulerian Snow on Sea Ice Model. The coarse resolution (~100 km) snow data are redistributed onto the high-resolution (approximately 30–100 m) ATL10 freeboards using relationships obtained from snow depth and freeboard data collected by NASA's Operation IceBridge mission. We present regional sea ice thickness distributions and highlight their seasonal evolution through our first winter season of data collection. We include ice thickness uncertainty estimates, while also acknowledging the limitations of these estimates. We generate a gridded monthly thickness product and compare this with various monthly sea ice thickness estimates obtained from European Space Agency's CryoSat-2 satellite mission, with ICESat-2 showing consistently lower thicknesses. Finally, we compare our February/March 2019 thickness estimates to ICESat February/March (19 February to 21 March) 2008 ice thickness estimates using the same input assumptions, which show an ~0.37 m or ~20% thinning across an inner Arctic Ocean domain in this 11-year time period.

**Plain Language Summary** NASA's ICESat-2 mission was launched in September 2018 with the primary goal of monitoring our rapidly changing polar regions. The sole instrument onboard is a highly precise laser, which is now providing routine, very high-resolution, surface height measurements across the globe, including over the Arctic and Southern oceans. In this study, we show new estimates of Arctic sea ice thickness from the first winter season of data collected by ICESat-2. Sea ice thickness is calculated by combining the measured ICESat-2 freeboards—the extension of sea ice above sea level—with a new snow on sea ice model. Our derived thicknesses are consistently lower than the thicknesses calculated from ESA's CryoSat-2 data and the original ICESat mission, which ended in 2008. More work is needed to verify these new thickness estimates.

## 1. Introduction

The Arctic and Southern oceans are blanketed by a layer of sea ice that modulates energy exchange between the atmosphere and ocean. The growth, transport, and melt of sea ice provide a significant source of seasonal freshwater flux into and out of the ocean, driving mixing and modulating ocean stratification (e.g., Aagaard & Carmack, 1989; Carmack et al., 2016; Serreze et al., 2006). Various biogeochemical cycles operate within sea ice and around its interface (Vancoppenolle et al., 2013 and references therein), while the presence of thick consolidated ice can provide a key platform for various species and local communities living within the Arctic. Monitoring the state of sea ice across the Polar oceans is thus a key priority of the Earth Science research community. Rapid declines in Arctic and Antarctic sea ice have further motivated improved understanding of sea ice variability and its myriad connections with the local and global climate and weather systems (e.g., Parkinson, 2019; Screen & Francis, 2016; Stroeve & Notz, 2018).

The National Aeronautics and Space Administration (NASA) Ice, Cloud, and land Elevation Satellite (ICESat) mission, launched in 2003 and operated until 2009, measured the Earth's surface elevation to a high precision using the onboard Geoscience Laser Altimeter System (Zwally et al., 2002). ICESat emitted 1,064-nm laser light 40 times per second and measured the round-trip time of flight of the laser pulses (Zwally et al., 2002). These times of flight are then converted to surface elevation measurements when combined with the observatory position and attitude. The laser pulses yielded approximately 70-m diameter footprints on the surface of the Earth spaced ~150 m along the single track. The relatively high precision of the elevation measurements enabled reliable estimates of sea ice freeboard—the extension of sea ice above a local sea surface (e.g., Kwok et al., 2007; Zwally et al., 2002; Zwally et al., 2008). Sea ice freeboard (centimeters to tens of centimeters) is converted to sea ice thickness (tens of centimeters to meters) using prerequisite assumptions including sea ice density and snow depth/density (e.g., Kurtz et al., 2011; Kwok & Cunningham, 2008). These freeboard and thickness estimates provided crucial additional information regarding the state of sea ice cover compared to the now routine measurements of sea ice concentration obtained by passive microwave sensing (Cavalieri et al., 1996; Comiso, 2000; Comiso et al., 1997; Lavergne et al., 2019; Meier et al., 2017; Parkinson et al., 1999). The full ICESat sea ice thickness record demonstrated a rapid thinning of the Arctic sea ice cover over this relatively short time period (Kwok et al., 2009), a period of transition in the Arctic which included the then record low summer sea ice extent of 2007 (Stroeve et al., 2008). The European Space Agency (ESA) launched the CryoSat-2 radar altimeter in 2010, which has provided the primary source of basin-scale coverage of Arctic sea ice thickness since the loss of ICESat (e.g., Kurtz et al., 2014; Kwok & Cunningham, 2015; Laxon et al., 2013; Ricker et al., 2017).

Following the success of ICESat, the National Research Council's 2007 Earth Science Decadal Survey recommended a follow-on mission to continue the time series of data enabled by ICESat, including sea ice thickness (National Research Council, 2007). Around 10 years later, on 15 September 2018, NASA's ICESat-2 mission was launched successfully from Vandenberg Air Force Base (Markus et al., 2017), with science quality data collected since 14 October 2018. These data are now being publicly disseminated through the National Snow and Ice Data Center (NSIDC; <https://nsidc.org/data/icesat-2>). The sole instrument onboard ICESat-2 is the photon-counting Advanced Topographic Laser Altimeter System (ATLAS). ATLAS uses a low pulse-energy laser split into a six-beam configuration of three beam pairs (a strong and a weak beam) compared to the single beam laser profiling of the original ICESat mission (Neumann et al., 2019). The introduction of multiple beam pairs was driven primarily by the needs of the ice sheet community, as this enables separation of elevation change from local surface slope. However, this novel multibeam configuration is also expected to be of utility for sea ice analyses through, for example, improved lead finding (the cracks between ice floes needed to derive the local sea level), assessments of spatial length scale variability, and beam consistency assessments. Another key advance of ICESat-2 is that at orbital velocities it generates individual laser footprints of ~14 m (in diameter) on the Earth's surface, with each footprint separated by only 70 cm, a much higher resolution and sampling than ICESat. ICESat-2 also samples year round, a significant improvement over the approximately two to three monthly campaign surveys conducted annually by ICESat.

A number of standard data products generated from ICESat-2 have recently been made available to the public through the NSIDC. For sea ice users, the primary data sets of interest include the individual photon cloud heights (ATL03, Neumann, Martino, et al., 2019; Neumann et al., 2019a; Neumann et al., 2019b) and the derived along-track sea ice/sea surface heights (ATL07, Kwok et al., 2019a) and freeboards (ATL10, Kwok et al., 2019b), which are available across both hemispheres. The production of ATL07 and ATL10 are described in detail in the Algorithm Theoretical Basis Document (Kwok et al., 2019) with initial results of the first growth season of data presented in Kwok et al. (2019). As ancillary data, mainly snow depth and density, are needed to estimate sea ice thickness from the IS-2 derived freeboards, sea ice thickness was not listed as a specific mission requirement (Markus et al., 2017). However, there is a clear community need for consistent and routine ICESat-2 sea ice thickness estimates to enable assessments of the state of the sea ice pack and to support efforts including climate model calibration/validation and data assimilation/seasonal forecast initialization (Allard et al., 2018; Blockley & Peterson, 2018; Lindsay et al., 2012; Petty et al., 2018; Schröder et al., 2019). It is also expected that such data can be used to assess sea ice thickness estimates derived from alternative satellite missions such as ESA's CryoSat-2. As such, the ICESat-2 Project Science Office based at NASA's Goddard Space Flight Center (GSFC) has developed

a new processing chain to convert the ATL10 freeboards into sea ice thickness, which we plan to deliver routinely to the public at a similar latency to the release of ATL10 freeboard data.

We focus our initial efforts on the Northern Hemisphere (Arctic Ocean) due primarily to our more advanced, but still somewhat limited, knowledge of snow on sea ice compared to the Southern Hemisphere (Southern Ocean) and due to the availability of coincident CryoSat-2 ice thickness estimates. We use ATL10 data from 14 October 2018 through to 30 April 2019, which are publicly available through the NSIDC (<https://nsidc.org/data/atl10>). Our expectation is that our sea ice thickness product will initially only be produced through the annual winter/early spring period (e.g., 1 October to 30 April) due to the potential complexity of surface melt affecting the derivations of surface returns from ICESat-2 (e.g., the challenge of distinguishing melt ponds from leads) and the lack of snow data available during late spring/summer.

The main objectives of this paper are to describe the approach taken to estimate sea ice thickness with IS-2, highlight the seasonal/regional variability in our estimated ice thicknesses, and to compare these new thickness estimates with Arctic sea ice thickness data produced using CryoSat-2 and ICESat freeboard data. We acknowledge that a more complete comparison/calibration effort is needed, along with comparisons with airborne data collected by NASA's Operation IceBridge. In the following sections, we describe the ATL10 freeboard data, the ancillary snow on sea ice data utilized here (section 2), and our approach used to convert freeboard to thickness (section 3). We demonstrate the production of along-track and gridded fields of sea ice thickness data, highlight the regional and seasonal variability in these fields, and compare with coincident estimates from CryoSat-2 data and previous ICESat data (section 4). We conclude by discussing our future processing and research priorities (section 5).

## 2. Data

### 2.1. ICESat-2 Sea Ice Freeboard (ATL10)

We use the ICESat-2 ATL10 sea ice freeboard product (designated Release 002), which is disseminated through the NSIDC (Kwok, Cunningham, Markus, et al., 2019b, <https://nsidc.org/data/atl10>). The ATL10 freeboard product is the end result of a comprehensive series of algorithms and data products that, put simply, converts the latitude, longitude, and heights of individual photons detected by the orbiting ATLAS sensor; distinguishes signal photons from background photons; and produces a relative surface elevation of the sea ice or sea surface for each of the six laser beams. The six beams are comprised of three beam pairs, with each beam pair containing strong and weak beams that are separated by 90 m across track and 2.5 km along track, with each beam pair then separated by  $\sim 3.3$  km across track. Approximately every 9 months, the observatory switches orientation to maximize the sun angle incidence on the solar arrays and the labeling of the beams switches accordingly (see Figure 2 on the ATL07 product description for the beam configuration schematic; <https://nsidc.org/data/atl07>). The photon rates of the strong beam are roughly four times higher than those of the weak beam. Details on the production of individual photon cloud elevations can be found in the Level 2 ATL03 product description and initial paper summary (Neumann, Brenner, et al., 2019a; Neumann, Martino, et al., 2019).

For sea ice profiling, individual segment heights are produced from each beam using 150-photon aggregates in an effort to produce heights with a precision of  $\sim 2$  cm or less over flat surfaces, as described in the ATL07 sea ice/sea surface height product description and Algorithm Theoretical Basis Document (Kwok, Cunningham, Hancock, et al., 2019; Kwok, Cunningham, Markus, et al., 2019a). This results in segment lengths of  $\sim 10$  to 200 m for the strong beam (mean of  $\sim 15$  m) and  $\sim 40$  to 800 m (mean of  $\sim 60$  m) for the weak beam (Kwok, Cunningham, Hancock, et al., 2019). The individual laser footprint size of  $\sim 14$  m is added to the segment length to calculate the spatial resolution of the segments (i.e., a mean of  $\sim 30$  m for the strong beam and 75 m for the weak beam). For sea ice, one of the key challenges is distinguishing the segment height estimates from either the surface of sea ice or leads (cracks/openings between ice floes). A decision-tree algorithm is used to discriminate the returns between the following surfaces: smooth dark leads, rough dark leads, gray ice, snow-covered ice, rough ice, shadow, and specular returns. The photon rate, width of the Gaussian photon distribution, and calculated background rate are used as the input variables to this algorithm for each along-track height segment. Freeboards are calculated for all segments within 10-km along-track sections that include a segment height classified as an open water lead (all lead heights are used within each 10-km section). Differencing the heights of the sea ice surface from the local

sea surface heights (heights of the segments classified as leads) provides the estimate of freeboard given in ATL10. This is currently done individually for each beam, although the expectation is that a reference sea surface will be produced across the beams once all the beams are fully aligned, which is dependent on the eventual full calibration of the ATLAS instrument.

In this version (Release 002) of ATL10 data, freeboards are only produced in regions greater than 50 km away from the nearest coastline and with an ice concentration above 50% (derived from the Multisensor Analyzed Sea Ice Extent-Northern Hemisphere product; Fetterer et al., 2010) to avoid potential issues with tides and ocean waves. In this study, we only use the strong beams (Beam 1, 3, and 5), as these provide higher along-track resolutions than the weak beams (Beams 2, 4, and 6) due to their higher signal photon rates. We primarily use just one of the strong beams (Beam 1) for simplicity in this initial study but also show thickness comparisons across the three strong beams to further demonstrate the interbeam consistency. The ATL10 data are provided in individual granules for a given Northern (or Southern) Hemisphere crossing (containing all the data for the six beams) in the Hierarchical Data Format–version 5 format. Regional ATL10 freeboard distributions across the entire 2018/2019 winter season are given in Supporting Information Figure S1.

## 2.2. Snow Loading

One of the main challenges in converting sea ice freeboard to thickness is uncertainty in snow loading. There is no community consensus regarding the most reliable basin-scale snow depth and density product available, so here we use data from a new snow reconstruction and a commonly used climatology, together with a methodology to redistribute these coarse snow data to high resolution (section 3.1.1).

### 2.2.1. NESOSIM

We primarily make use of snow depth and density data from the NASA Eulerian Snow On Sea Ice Model (NESOSIM) v1.0, a new open-source snow budget model that is currently configured to simulate snow on sea ice across the Arctic Ocean through the accumulation season (Petty, Webster, et al., 2018). NESOSIM has been developed in a three-dimensional Eulerian framework and includes two (vertical) snow layers and several simple parameterizations (accumulation, wind packing, advection-divergence, and blowing snow lost to open water/leads) to represent key sources and sinks of snow on sea ice. The data are provided daily from 15 August through to 1 May at a horizontal resolution of  $100 \times 100$  km. The model is forced with the European Centre for Medium-Range Weather Forecasts ERA-Interim (ERA-I) snowfall and winds (Dee et al., 2011), NASA Climate Data Record (CDR) sea ice concentrations (Meier et al., 2017), and the European Organization for the Exploitation of Meteorological Satellites (EUMETSAT) Ocean and Sea Ice Satellite Application Facility (OSI SAF, [www.osi-saf.org](http://www.osi-saf.org)) ice drifts (Lavergne et al., 2010), which are all regridded to the  $100 \times 100$ -km Arctic Ocean grid. ERA-I snowfall-forced simulations produced the best comparisons with snow depth data collected by NASA's Operation IceBridge compared to several other reanalyses (Petty, Webster, et al., 2018), although the model was calibrated with this same forcing data. ERA-I data are available with an approximately 2-month latency. CDR ice concentrations and OSI SAF ice drifts are near real-time products chosen primarily due to data latency considerations. NASA Team concentrations are also available near real time (Maslanik & Stroeve, 1999) but tend to show a low bias compared to other concentration products (e.g., Meier, 2005). Initial (15 August 2018) conditions are calculated using a scaled climatology based on the duration of ERA-I near-surface (2 m) air temperatures above freezing, as described in Petty, Webster, et al. (2018). The NESOSIM snow depths/densities for 15 October 2018, 15 January 2018, and 15 April 2019 are shown in Figures S2–S4. Monthly maps of winter 2018/2019 NESOSIM snow depths across the Arctic are included in the main results (section 4). ERA-I was superseded by ERA5 in August 2019, and we discuss the implications for future snow depth and ice thickness retrievals in section 5.2.

### 2.2.2. Warren Snow Climatology

We also utilize a commonly used climatology of snow depth and density based on a simple quadratic functional fit to Soviet drifting station data collected prior to 1991 (Warren et al., 1999, referred to herein as W99). The W99 snow density climatology provides the only observationally based basin-scale assessment of snow density currently available. This snow climatology is expected to be outdated, however, due to the rapid changes experienced in the Arctic climate system over the last few decades (Webster et al., 2014). We thus follow other recent studies that have modified the snow depth climatology based on satellite-derived ice type classification (a scaling factor of 50% and 70% of the

climatology over first-year ice [FYI], e.g., Laxon et al. (2013); Kwok & Cunningham, 2015). We use just the 50% snow depth scaling over FYI, referred to herein as W99m5. We use the EUMETSAT OSI SAF sea ice type product that is derived from a combination of passive microwave and scatterometry data at 10-km horizontal resolution to discriminate FYI from multiyear ice (MYI) (Breivik et al., 2012). No ice type scaling is applied to the snow density estimates.

Our inclusion of the W99 climatology snow loading is also motivated by our CryoSat-2 thickness comparisons and expected efforts to reconcile this sea ice thickness data set with data produced from alternative (previous and ongoing) satellite altimetry missions and its potential utility in the production of a rapid-release data product (discussed later). The W99m5 snow depths are used in the Alfred Wegener Institute (AWI) and NASA (GSFC and Jet Propulsion Laboratory [JPL]) comparisons. We also produce a mean monthly Warren snow depth climatology following the approach taken by Center for Polar Observation & Modelling (CPOM) (Tilling et al., 2018) whereby an Arctic Ocean region mask is used to derive a mean snow depth and density value, which is applied to all the segments classified as MYI based on the OSI SAF ice-type product, and a 50% scaled snow depth applied to all the FYI segments. These snow loading assumptions combined with the relevant sea ice density approximations used to produce comparison ICESat-2 thickness estimates are summarized in Table 1.

In comparisons with snow depth data collected in spring from NASA's Operation IceBridge (OIB) airborne mission, both the NESOSIM (forced with ERA-I data) and W99m5 comparisons showed root mean squared errors of around 10 cm or better, depending on the year or OIB product analyzed. However, the W99m5 data exhibit an unphysical bimodal distribution in snow depth not shown in the spring OIB observations and provide no estimate of interannual variability, giving us more confidence in the NESOSIM results for capturing the full spatial and temporal variability in snow depth and thus ice thickness within a given Arctic winter (Bunzel et al., 2018).

### 2.3. Sea Ice Density

Basin-scale estimates of sea ice density are very limited, due primarily to the challenges of in situ data collection and our lack of remote sensing capabilities. Sea ice thickness studies thus often utilize a constant value of sea ice density, for example, a fixed density of  $915 \text{ kg m}^{-3}$ , based on historical in situ data collected in localized regions of the Arctic (Kurtz et al., 2014; Kwok & Cunningham, 2015). The Kwok and Cunningham (2015) study, the CPOM CS-2 thickness product (Laxon et al., 2013; Tilling et al., 2018), and the AWI CS-2 thickness product (Hendricks & Ricker, 2016) also use ice type to differentiate between an MYI density of  $882 \text{ kg m}^{-3}$  and a FYI density of  $917 \text{ kg m}^{-3}$  based on the analysis of airborne Sever expedition data (in situ data collected by drill holes prior to 1993) by Alexandrov et al. (2010). As discussed in Kwok and Cunningham (2015), the MYI currently observed in the Arctic is likely different (younger/thinner and thus probably of higher bulk density) than the ice profiled during the airborne Sever expeditions, so this approach could represent a lower bound of ice density assumptions. However, in situ ice density data collection is challenging, and while studies suggest the density of the MYI above sea level may well be lower (the brine has had longer to drain or be flushed into the ocean), other studies have suggested minimal difference in density for the ice submerged below sea level (Timco & Frederking, 1996). We thus choose to utilize a fixed density of  $915 \text{ kg m}^{-3}$  for both ice types but also include the FYI/MYI density assumption in our estimates of systematic errors (discussed in section 3.2) and in our CS-2 comparisons (next section).

### 2.4. CryoSat-2 Sea Ice Thickness

We compare our IS-2 thicknesses with thickness estimates obtained from the ESA's CryoSat-2 (CS-2) radar altimeter, which was launched in April 2010 (Wingham et al., 2006). CS-2 provides estimates of ice freeboard, the extension of sea ice (not including its overlying snow cover) above sea level, which is converted to sea ice thickness using similar assumptions of snow depth, snow/ice density, and hydrostatic equilibrium (described in section 3). As the radar signal is thought to penetrate through the snow layer toward the snow-ice interface, a speed of light correction is also applied, which is a function of the estimated snow depth and density. As mentioned already, several international groups currently generate CS-2 thickness estimates, but here, we use data from the NASA's GSFC (Kurtz & Harbeck, 2017), the JPL (Kwok & Cunningham, 2015), the CPOM Laxon et al., 2013, Tilling et al., 2018), and the AWI (Hendricks & Ricker, 2016). As the different products make different assumptions regarding snow loading and sea ice

**Table 1**  
*Sea Ice Thickness Input Assumptions*

Thickness label	Snow depth	Snow depth redistribution	Snow density	Sea ice density (kg/m <sup>3</sup> )
NS	NSIM	-	NSIM	915
NS <sub>rd-pw</sub>	NSIM	piecewise	NSIM	915
NS <sub>rd-pw-rho2</sub>	NSIM	piecewise	NSIM	917 (FYI) 882 (MYI)
NS <sub>rd-pw-rho3</sub>	NSIM	piecewise	NSIM	917 (FYI) 899 (MYI)
NS <sub>rd-sig</sub>	NSIM	sigmoid	NSIM	915
W99m5	W99m5 (50% scaling over FYI)	-	W99	915
W99m5 <sub>rd-pw</sub>	W99m5 (50% scaling over FYI)	piecewise	W99	915
CPOM	W99m5r (50% scaling over FYI, monthly ice type means)	-	W99 (monthly ice type means)	917 (FYI) 882 (MYI)
AWI	W99m5 (50% scaling over FYI)	-	W99	917 (FYI) 882 (MYI)
NASA	W99m5 (50% scaling over FYI)	-	W99	915

Note. FYI, First-year ice, MYI, Multi-year ice, NSIM, NESOSIM.

density, we replicate these in distinct IS-2 thickness estimates to provide more direct comparisons (these input assumptions are summarized in Table 1). We note again that a more detailed assessment exploring the multiple CS-2 products is needed, which is beyond the scope of this study, so we instead view this as an initial comparison rather than a complete calibration/validation analysis.

### 2.5. ICESat Sea Ice Freeboard

We use ICESat freeboard data from the February/March campaign periods (FM03: 20 February to 29 March 2003; FM04: 17 February to 21 March 2004; FM05: 17 February to 24 March 2005; FM06: 22 February to 27 March 2006; and FM08, 17 February to 21 March 2008) as described in Kurtz et al. (2011), which are processed following the methodology of Kwok et al. (2007). ICESat data have a footprint size of ~70 m, an along-track spacing of 150 m, and coverage up to 86°N. These freeboard data are only produced for ice concentrations greater than 50%, as in ATL10 but taken from NASA Team passive microwave data (Cavalieri et al., 1996). In this study, we convert the ICESat freeboards into thickness using the same piecewise redistributed NESOSIM snow loading (NS<sub>rd-pw</sub>).

### 2.6. Ancillary Data

We use the EUMETSAT OSI SAF sea ice type product (Breivik et al., 2012) to delineate our results between FYI and MYI. We also utilize the NSIDC regional mask of the Arctic Ocean and its peripheral seas to delineate the results by Arctic region. We analyze results in the Central Arctic, Beaufort Sea, Chukchi Sea, East Siberian Sea, Laptev Sea, Kara Sea, and Barents Sea and also an “Inner Arctic” domain that includes the Central Arctic, Beaufort, Chukchi, East Siberian, and Laptev seas. A map of these regions is shown in Figure S5.

## 3. Methods

### 3.1. Sea Ice Thickness Processing

Sea ice thickness can be calculated from the total ice freeboard provided by ATL10,  $h_f$ , assuming hydrostatic equilibrium as

$$h_i = \frac{h_f \rho_w}{(\rho_w - \rho_i)} + \frac{h_s (\rho_s - \rho_w)}{(\rho_w - \rho_i)}, \quad (1)$$

where  $\rho_w$  is the density of water (which we take to be 1,024 kg m<sup>-3</sup>),  $h_s$  and  $\rho_s$  are the variable snow depth and density, respectively, and  $\rho_i$  is the bulk density of sea ice (see Figure 1 for a basic schematic). Below, we provide the description of these input assumptions, including the snow depth/density and sea ice density, and efforts to redistribute the coarse input snow depths to the high resolution of the ICESat-2 freeboard measurements. We also present thickness uncertainty estimates and describe the production of along-track and gridded sea ice thickness data products. A schematic of the complete processing chain is given in Figure 2.

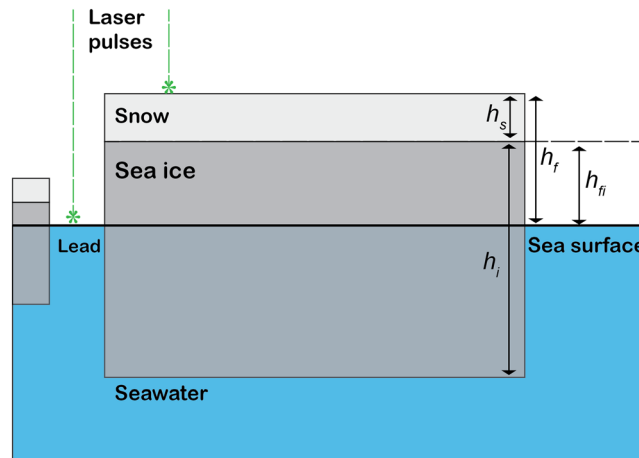


**Figure 1.** Schematic of a snow-covered sea ice floe in hydrostatic equilibrium and the main variables being utilized in this study to derive sea ice thickness.  $h_s$ : snow depth,  $h_r$ : total freeboard,  $h_{fi}$ : ice freeboard, and  $h_i$ : sea ice thickness.

Note that this assumption of isostasy is thought to be more questionable in regions of high ice concentration and deformation (e.g., within and around the Canadian Arctic Archipelago) at the kinds of segment length scales of ATL10 (tens to hundreds of meters) (Doble et al., 2011). The use of a 50-km coastal mask in the ATL10 data mitigates this to some degree but is still something to consider when assessing the raw along-track thickness estimates in high ice concentration regimes.

As discussed in Kwok, Markus, Kurtz, et al. (2019), it is important to take into account the variable height segment length in any statistical analyses of these data, for example, by weighting the data based on the segment length, thus a mean thickness within a given area can be determined as

$$\bar{h}_i = \frac{\sum_N h_i^i L_s^i}{\sum_N L_s^i}, \quad (2)$$

where  $h_i^i$  is the thickness of a given segment,  $L_s^i$  is the segment length, and  $N$  is the number of segments in a given area/bin/grid cell.

### 3.1.1. Snow Depth Redistribution

As discussed in section 2, we use snow loading data from NESOSIM v1.0 (Petty, Webster, et al., 2018) and also utilize the W99m5 snow climatology. We are not only limited in our confidence in the climatology or simulations/reconstructions of basin-scale snow depth available due primarily to the lack of validation data (as discussed in Petty, Webster, et al., 2018), but we are also limited by the resolution of these input data. NESOSIM, for example, provides data at a 100 km horizontal resolution while the W99 climatology is calculated using in situ data binned into sections of  $O(100 \text{ km})$  in size. Both are significantly larger than the freeboard segment resolution from ATL10 (approximately 30–200 m). To address these large differences in spatial scales, redistribution functions have been employed in the past to crudely represent small-scale variability not captured in the large-scale models/reconstructions, such as ice divergence/new ice formation in leads and wind redistribution, which tend to reduce the snow depth over younger/thinner ice floes. A method for redistributing coarse snow depths to the spatial scales relevant for ICESat was applied in Kwok and Cunningham (2008) and in Kurtz et al. (2009). Kwok and Cunningham (2008) used a sigmoidal function that was a function of the large-scale snow depth and the high-resolution freeboard, while Kurtz et al. (2009) used an empirical approach of fitting a piecewise function that was determined based on a limited set of airborne measurements taken near coastal Alaska in March 2006 (Cavalieri & Markus, 2003). The piecewise function calculated a snow depth that increased linearly with freeboard until reaching a certain cut-off value, at which point, a constant snow depth was assigned. Here, we expand on the empirical approach by utilizing data from the much more spatially and temporally extensive OIB flights taken from 2009–2018 to update the regression coefficients, ensure applicability to the smaller ICESat-2 footprint, and briefly explore alternative fitting procedures.

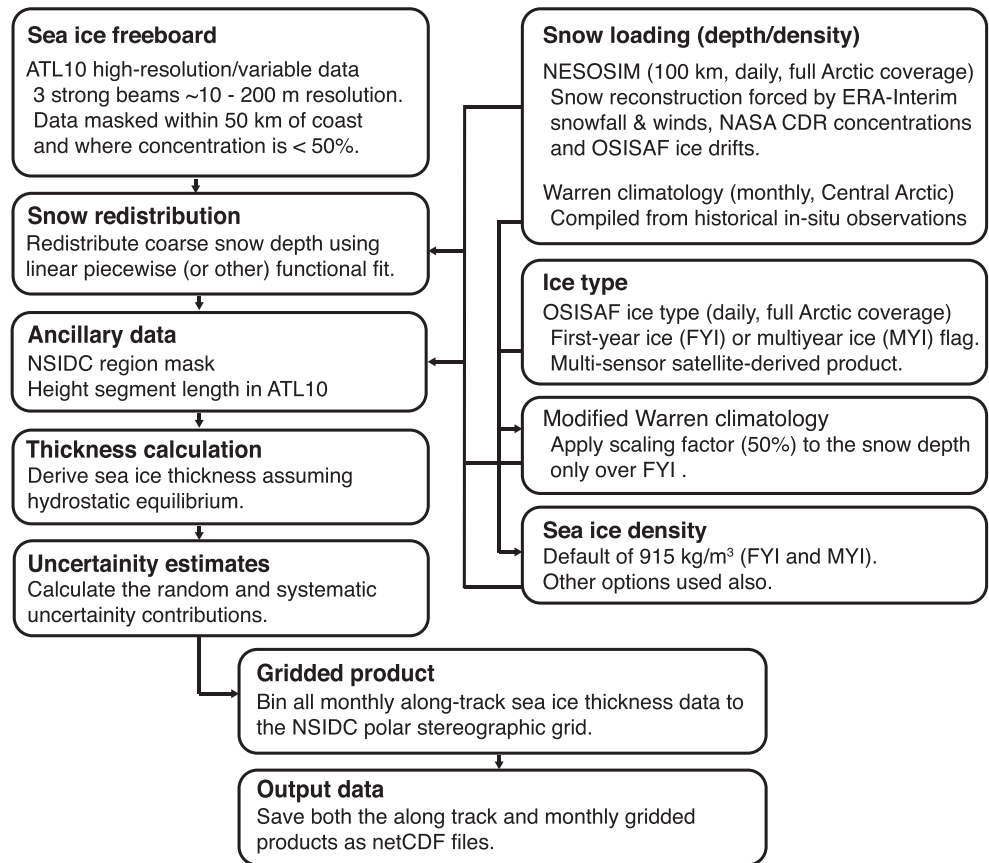


Figure 2. ICESat-2 sea ice thickness processing flowchart.

Our analysis using OIB snow depth and freeboard data suggests the linear piecewise function still provides our best guess at this functional form compared to our other possible options and improves the ability to reproduce a full sea ice thickness distribution with Operation IceBridge data compared to using a constant, large-scale snow depth value. The comparisons with other possible functional fits are described in more detail in Text S1. The linear piecewise function for estimating snow depth within a given 100-km (NESOSIM resolution) section at the scale of the ICESat-2 segment length is given as

$$h_s = \begin{cases} \frac{h_f}{h_{f\text{-cutoff}}} h_{s\text{-thick}}, & h_f < h_{f\text{-cutoff}} \\ h_{s\text{-thick}}, & h_f > h_{f\text{-cutoff}} \end{cases}, \quad (3)$$

where the freeboard cut-off value,  $h_{f\text{-cutoff}}$ , and snow depth cut-off for high freeboards,  $h_{s\text{-thick}}$ , are found from the linear regression functions

$$h_{f\text{-cutoff}} = c_1 h_{sl} + c_2 h_{fl} + c_3, \quad (4)$$

$$h_{s\text{-thick}} = c_4 h_{sl} + c_5, \quad (5)$$

where  $h_{sl}$  is the large-scale (100 km) mean snow depth,  $h_{fl}$  is the mean freeboard measured over the same length scale, and  $c_1$  to  $c_5$  are regression coefficients ( $c_1 = 0.70$ ,  $c_2 = 0.22$ ,  $c_3 = 0.16$  m,  $c_4 = 1.03$ , and  $c_5 = 0.01$  m) calculated from the OIB data. As a final step, the large-scale mean snow depth within a given 100-km section is conserved through an iterative adjustment (maximum of 10 iterations) of  $h_{s\text{-thick}}$  such that the mean of  $h_s$  along the altimeter track is within 1 cm of  $h_{sl}$ . The benefit of the snow redistribution is demonstrated in Figure 3, which shows the thickness distribution using a constant, or redistributed snow depth, compared to the actual thickness distribution calculated by OIB data. Note that we also produce high-resolution snow depth estimates using the sigmoid function used in Kwok and Cunningham (2008) to enable potential comparisons with those data and to assess the sensitivity to the chosen redistribution

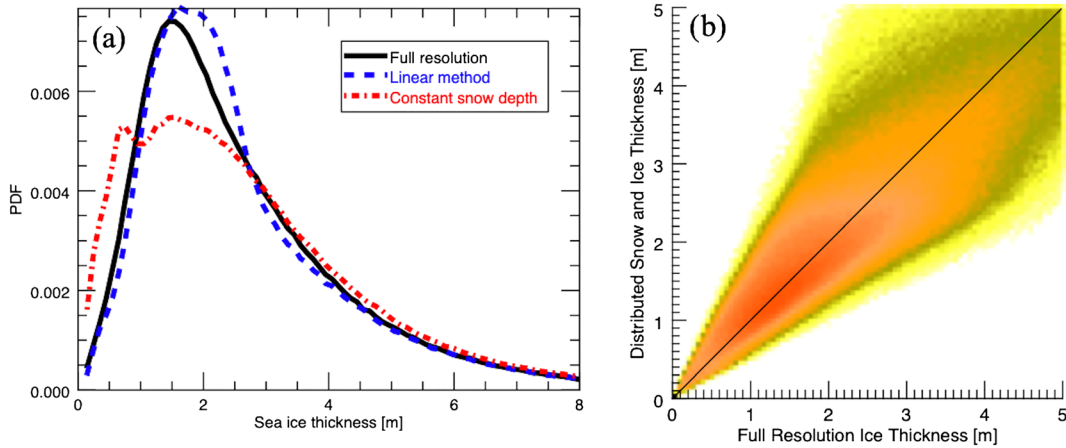


**Figure 3.** Arctic sea ice thickness distribution calculated using a piecewise snow redistribution of large-scale snow depths/freeboards from NASA's Operation IceBridge data (2010–2018). (Left) Black line shows the IceBridge thickness product distribution, the red line shows the thickness using constant 100-km mean OIB snow depths, and the blue line shows the thickness distribution calculated using a linear piecewise redistribution of the mean 100 km snow depth; and (right) heat map of the difference between the piecewise redistribution thickness estimates and the raw thickness estimates.

procedure. This sigmoid functional redistribution does not attempt to conserve snow mass (no iterative adjustment), following Kwok and Cunningham (2008), as this was seen to represent a physical sink of snow through small-scale dynamics.

### 3.2. Sea Ice Thickness Uncertainty Estimates

We provide uncertainty estimates for our individual ice thickness estimates. Providing ice thickness uncertainties is challenging due to the general lack of validation data and poor constraints on the uncertainties of the individual terms contributing to the total ice thickness estimate. Here, we provide estimates of the random uncertainties and systematic uncertainties that contribute to the total thickness uncertainty estimate. To calculate the random uncertainty, we combine the partial derivatives of the unconstrained variables featured in the hydrostatic equilibrium equation (equation 1) with estimates of the individual error terms, as discussed in more detail in Ricker et al. (2014) for radar altimetry of sea ice thickness. For laser altimetry, this total random uncertainty,  $\epsilon_r$ , can thus be expressed as

$$\begin{aligned} \epsilon_r^2 = & \epsilon_{h_f}^2 \left( \frac{\rho_w}{(\rho_w - \rho_i)} \right)^2 + \epsilon_{h_s}^2 \left( \frac{\rho_s}{(\rho_w - \rho_i)} - \frac{\rho_w}{(\rho_w - \rho_i)} \right)^2 + \epsilon_{\rho_s}^2 \left( \frac{h_s}{(\rho_w - \rho_i)} \right)^2 \\ & + \epsilon_{\rho_i}^2 \left( \frac{h_f \rho_w}{(\rho_w - \rho_i)^2} + \frac{h_s \rho_s}{(\rho_w - \rho_i)^2} - \frac{h_s \rho_w}{(\rho_w - \rho_i)^2} \right)^2, \end{aligned} \quad (6)$$

where  $\epsilon_{h_f}$  is the freeboard uncertainty,  $\epsilon_{h_s}$  is the snow depth uncertainty,  $\epsilon_{\rho_s}$  is the snow density uncertainty, and  $\epsilon_{\rho_i}$  is the sea ice density uncertainty (Giles et al., 2007). We assume the uncertainty introduced from sea water density uncertainty is negligible. The freeboard uncertainty,  $\epsilon_{h_f}$ , is variable and is calculated as the sum of the freeboard segment height spread given in ATL10 (the width of the Gaussian fit to the individual photon heights within each segment) and 2 cm, the expected precision of ATLAS over level ice surfaces at the segment length scale (Kwok, Markus, Kurtz, et al., 2019). The snow depth uncertainty,  $\epsilon_{h_s}$ , we estimate following the redistribution analysis described earlier, by evaluating the difference between the piecewise functional fit and the raw OIB snow depths. This uncertainty was found to be a clear function of freeboard and is given as  $\epsilon_{h_s} = 0.2h_f + 0.01$  m. The snow density error,  $\epsilon_{\rho_s}$ , we take to be a constant of  $40 \text{ kg m}^{-3}$  based on Warren et al. (1999). The sea ice density error,  $\epsilon_{\rho_i}$ , we take to be a constant of  $10 \text{ kg m}^{-3}$  based on Alexandrov et al. (2010). We provide these uncertainties at the individual segment scale but assume that as they are random errors, they reduce significantly and become negligible when averaged/binning into a gridded 25-km thickness uncertainty, an assumption discussed later.

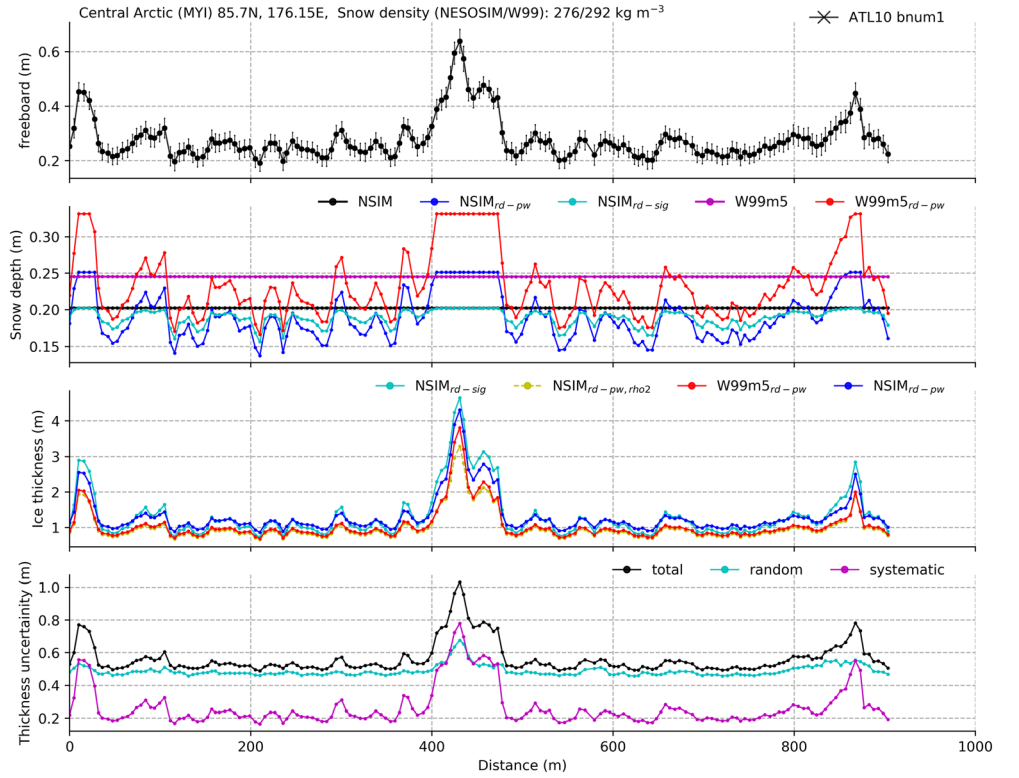


**Figure 4.** (Top row) ATL10 freeboards from the strong Beam 1 (gt3r in this orbit cycle) for a small (~1 km) profile within the Central Arctic Ocean on 16 November 2018 (location given by the star marker in Figure 6). The horizontal bars show the estimated freeboard uncertainty; (second row) coincident snow depths from NESOSIM (black), piecewise redistributed NESOSIM (blue), sigmoid redistributed (cyan), W99 (magenta), piecewise redistributed W99 (red); (third row) derived sea ice thickness using the ATL10 freeboards and the relevant snow depth assumptions; and (bottom row) thickness uncertainty estimates (total), estimates from the systematic, and random uncertainty assumptions.

We assume the above uncertainties represent the random, largely uncorrelated uncertainties but also attempt to provide estimates of the correlated, systematic uncertainties, which we calculate using the spread in available input assumptions. We thus calculate the systematic uncertainty estimate,  $\epsilon_s$ , as

$$\epsilon_s^2 = \epsilon_{h_s}^2 \left( \frac{\rho_s}{(\rho_w - \rho_i)} - \frac{\rho_w}{(\rho_w - \rho_i)} \right)^2 + \epsilon_{\rho_s}^2 \left( \frac{h_s}{(\rho_w - \rho_i)} \right)^2 + \epsilon_{\rho_i}^2 \left( \frac{h_f \rho_w}{(\rho_w - \rho_i)^2} + \frac{h_s \rho_s}{(\rho_w - \rho_i)^2} - \frac{h_s \rho_w}{(\rho_w - \rho_i)^2} \right)^2, \quad (7)$$

where  $\epsilon_{h_s}$ ,  $\epsilon_{\rho_s}$ , and  $\epsilon_{\rho_i}$  are calculated as the standard deviation in the various (redistributed) snow depth, snow density, and ice density assumptions described above. We expect that these uncertainties are highly correlated and thus do not reduce as we aggregate/bin the data so use these uncertainties solely in our gridded monthly sea ice thickness uncertainty. We provide this as a first uncertainty assessment but expect that a more complete assessment of the possible input assumptions will help further constrain this possible uncertainty, along with better understanding the contribution from uneven spatial sampling.

## 4. Results and Discussion

### 4.1. Example Profiles

Figures 4 and 5 provide two examples of our sea ice thickness processing chain over 1-km profiles of the MYI of the Central Arctic and the FYI of the Kara Sea, respectively. In both cases, the freeboards are taken from the ATL10 strong Beam 1 in cycle 1 (GT1R, the labeling depends on the orientation of the IS-2 observatory, which changes every few months to optimize sun angle, as discussed in section 2).

MYI profile in the Central Arctic on 16 November 2018 (Figure 4): the ATL10 freeboards in this approximately 1-km profile vary between ~0.2 and 0.6 m. The peaks in freeboard (at ~20, 420, and 900 m) are

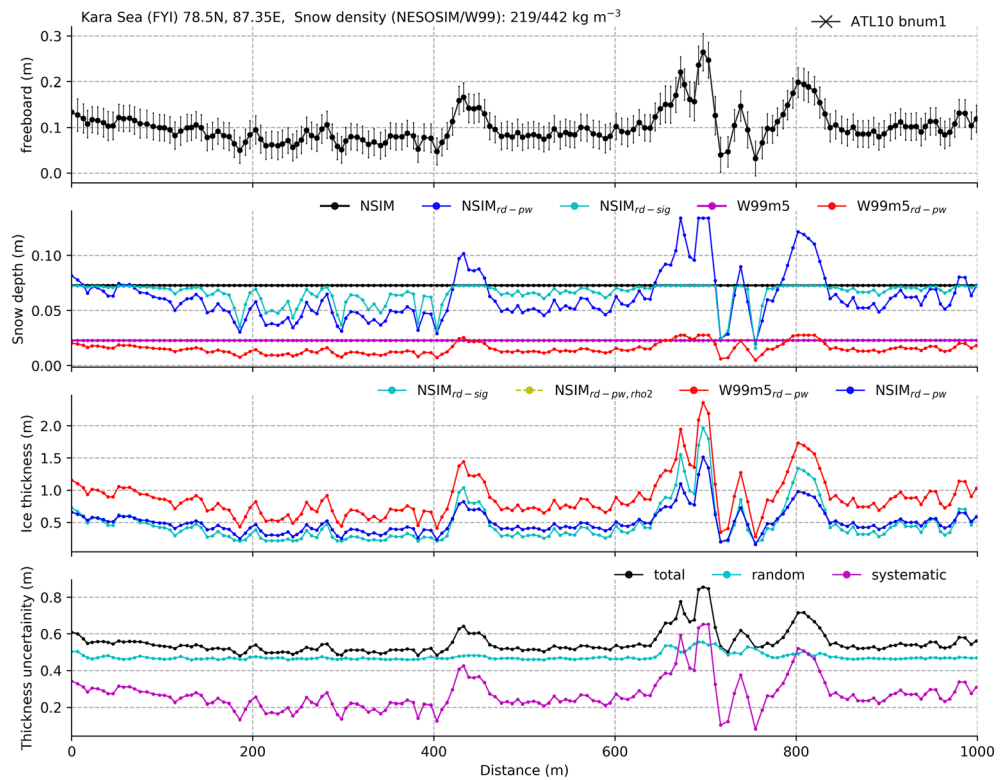


**Figure 5.** As in Figure 4 but for an FYI profile in the Kara Sea on 18 November 2018 (location given by the triangle marker in Figure 6).

likely a result of pressure ridging driving vertical redistribution of ice in this region known to undergo such deformation. Snow features such as sastrugi and dunes are another possible cause of small-scale topography/freeboard variation (Thomas & Dieckmann, 2009), although it is rare for these features to extend much beyond a few tens of centimeters from the ice surface (e.g., Warren et al., 1999). Also shown are the various coincident snow depth assumptions, including the coarse (not redistributed) NESOSIM and modified Warren snow depths (W99m5) and the redistributed piecewise and sigmoid snow depths described above. Note that as this profile is in the MYI zone, the W99m5 snow depths have not been modified from their original climatology value. The coincident NESOSIM and W99 snow depths across this 1-km profile are 20 and 25 cm, respectively. In the mass conserved piecewise redistribution, we see clearly the snow depths covarying with the small-scale freeboard variability as expected from this functional form, with the snow depths oscillating around the raw constant value. The sigmoid function instead results in a decline in snow depth for the lower freeboards only, resulting in a net sink of snow. As discussed earlier, the rationale of this redistribution approach is that the sink represents small-scale physics such as ice/snow divergence and new and later ice formation in leads not included in snow reconstructions/climatologies. The ice thickness derived from these freeboards and snow depth (and constant snow densities of 272 and 292 kg m<sup>-3</sup> for NESOSIM and W99, respectively) vary from ~1 m for the lowest freeboards up to ~2 to 4 m for the high topography features. We also show the thickness derived using the piecewise redistributed NESOSIM data but using the two MYI ice density approximation (882 kg m<sup>-3</sup> for MYI, NS<sub>rd-rho2</sub>), which results in thinner ice due to the lower ice density assumptions. Our estimates of ice thickness uncertainty are also included, which, as described in section 3, are a combination of the random and systematic uncertainties. In this example, the random uncertainty is consistently higher than the systematic uncertainty, with the total thickness uncertainty varying from ~0.5 m (~40–50% of the ice thickness) to ~1 m for the thickest ice (~25%). It is worth noting again that these uncertainty estimates are relatively crude approximations that we hope to assess and improve in future analyses, for example, by validating the thickness estimates with direct (e.g., airborne or in situ) thicknesses to provide more direct uncertainty estimates.

FYI profile in the Kara Sea on 18 November 2018 (Figure 5): as expected from this FYI profile in this more peripheral Arctic Ocean region, the freeboards are lower than the example in Figure 4 and instead vary between  $\sim 0.05$  and  $0.25$  m. The profile shows an interesting high variability section at around  $700$  m from the start of the profile, which could be an example of ice divergence between two floes and the impact of raised flow edges from pressure ridging, an interesting, albeit speculative demonstration of the capability of ICESat-2. The rest of the profile exhibits the expected low height variability of relatively flat, new ice. Here, the raw NESOSIM snow depth is higher than W99m5 ( $8$  cm compared with  $2$  cm), with the redistribution providing the expected addition of small-scale variability based on the freeboard variability. Both snow depths are lower than the MYI example in Figure 4, as expected. The snow densities vary more considerably however, (snow densities of  $219$  and  $441$   $\text{kg/m}^3$  for NESOSIM and W99, respectively) which is not surprising considering the questionable validity of both snow depth assumptions due to the lack of validation data and poor knowledge of the snow densification, especially in these regions. The resulting thicknesses vary from  $\sim 0.3$  to  $2$  m but are generally around  $0.5$  to  $1$  m depending on the snow input assumptions used. In this example profile, our total uncertainty amounts to  $\sim 30$ – $100\%$  of the total thickness, although this is before any spatial averaging is carried out, which should reduce/eliminate the random error contribution.

#### 4.2. Spatial Variability in Winter Freeboard, Snow Depth, and Ice Thickness

The monthly maps of ATL10 freeboards from strong Beam 1, coincident redistributed NESOSIM snow depths, and our estimates of sea ice thickness across the 2018/2019 Arctic winter season are shown in Figures 6 (October, November, and December) and 7 (January, February, March, and April). The monthly mean sea ice extent derived from NASA CDR ice concentrations (15% concentration contour) is shown to demonstrate the high spatial coverage achieved from this early release (Release 002) of ICESat-2 data. The monthly (middle day of the month) MYI/FYI type contours from the OSI SAF product are also included, with more detailed ice type distributions shown later. It is worth noting that the October data are only available for the second half of the month, when routine data collection from IS-2 and sea ice growth began, so these monthly results will be biased high and should be viewed with caution when comparing to other months/data sets.

Across all months the freeboards, snow depth and ice thickness all show a general increase toward the Greenland and Canadian Arctic coastline, as expected from this being a region of ice convergence and consistently older ice and snow (Maslanik et al., 2011; Kwok, 2015; Petty, Tsamados et al., 2016; Kwok et al., 2017; Petty, Webster, et al., 2018). The spatial variability in our estimates of sea ice thickness is entirely plausible, featuring thicknesses of less than  $0.5$  to  $1$  m in the newly formed FYI regions of the Beaufort/Chukchi and Eastern Arctic Ocean and  $\sim 2$  to  $3$  m in the older and more deformed MYI region of the Central Arctic. All quantities generally increase through continued ice growth and snow accumulation through winter, with significant regional variability imposed over this.

In October, we see evidence of the late sea ice freeze-up across the Eastern Arctic and the Chukchi/Bering Sea region (<http://nsidc.org/arcticseaicenews/2018/11/unusual-warmth-continues/>). In November, we see evidence of the increase in ice coverage toward the southern Arctic peripheral seas, including near-full coverage in the East Siberian Sea, Laptev Sea, and Barents Sea and also near complete coverage in Baffin Bay, all featuring low freeboards, snow depths, and ice thickness indicative of relatively new ice formation. In December, the coverage extends through the Bering Strait and also into Hudson Bay. Also noteworthy in December is the extended tail of higher freeboards through the southern Beaufort Sea, along with some evidence of higher snow depths, and higher ice thicknesses in the region, likely due to the anticyclonic drift of the Beaufort Gyre driving the import of thicker, older ice from the Central Arctic (e.g., Hutchings & Rigor, 2012; Kwok et al., 2013; Petty, Hutchings et al., 2016). In January, the ice extent and thickness coverage extend further south, including the northern Sea of Okhotsk and increased coverage through the Bering Sea, which also shows increasing freeboards and ice thickness. In section 4.3, we show binned thickness estimates, which enable us to produce monthly differences and estimate the spatial patterns of seasonal thickness change more quantitatively.

#### 4.3. Sea Ice Thickness Distributions

The seasonal evolution of the monthly freeboard, snow depth, and sea ice thickness distributions within an Inner Arctic domain (Central Arctic, Beaufort, Chukchi, East Siberian, and Laptev seas) is shown in Figure 8

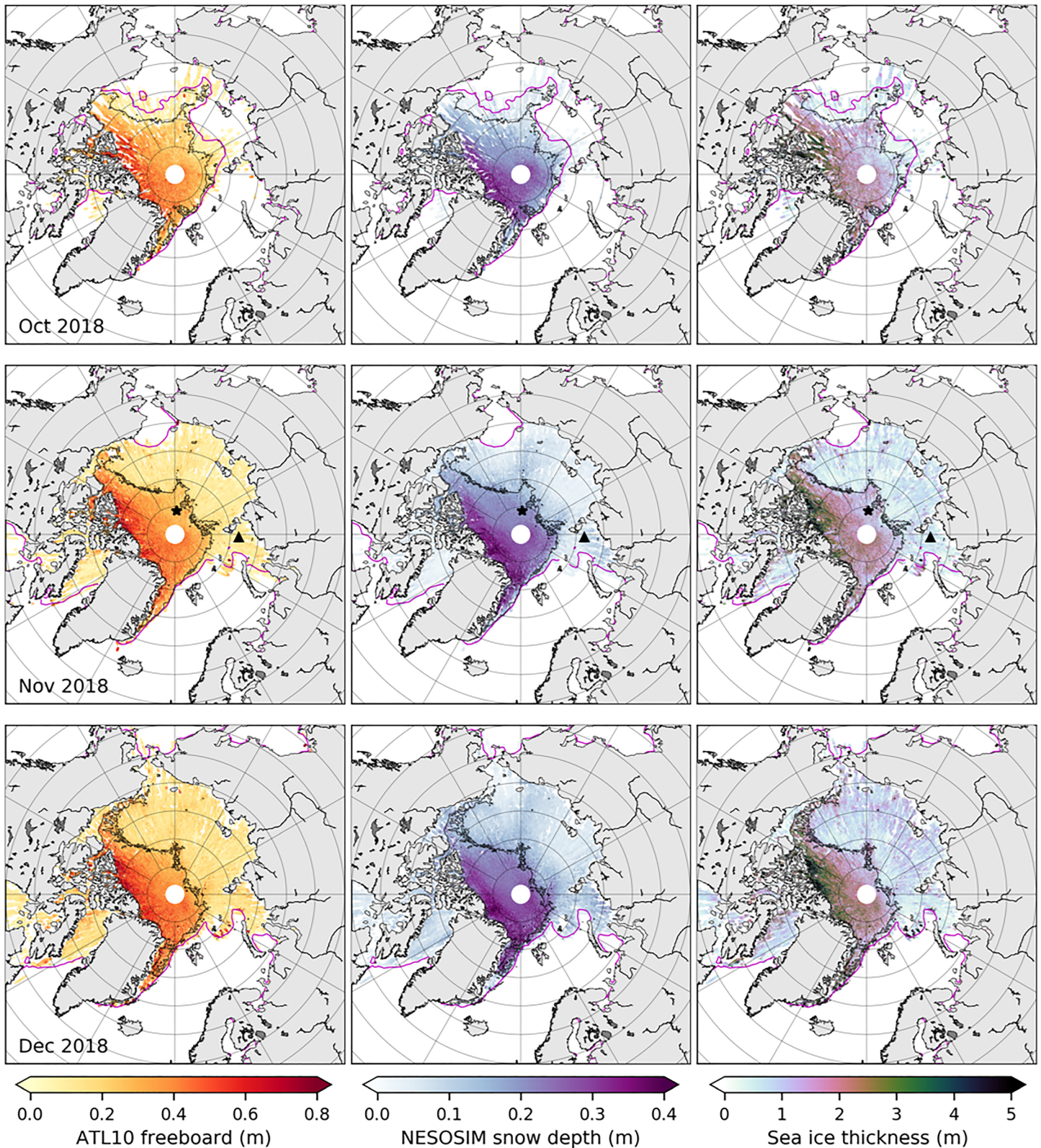


**Figure 6.** Monthly ATL10 freeboards, coincident NESOSIM (redistributed) snow depths and estimated sea ice thickness for October (top), November (middle), and December (bottom). The data are plotted using hexagonal bins. The magenta line is the 50% ice concentration contour from the CDR passive microwave data set, and the black line shows the first-year ice/multiyear ice boundary from the OSI SAF ice-type product. The star and triangle indicate the locations of the case studies shown in Figures 4 and 5, respectively.

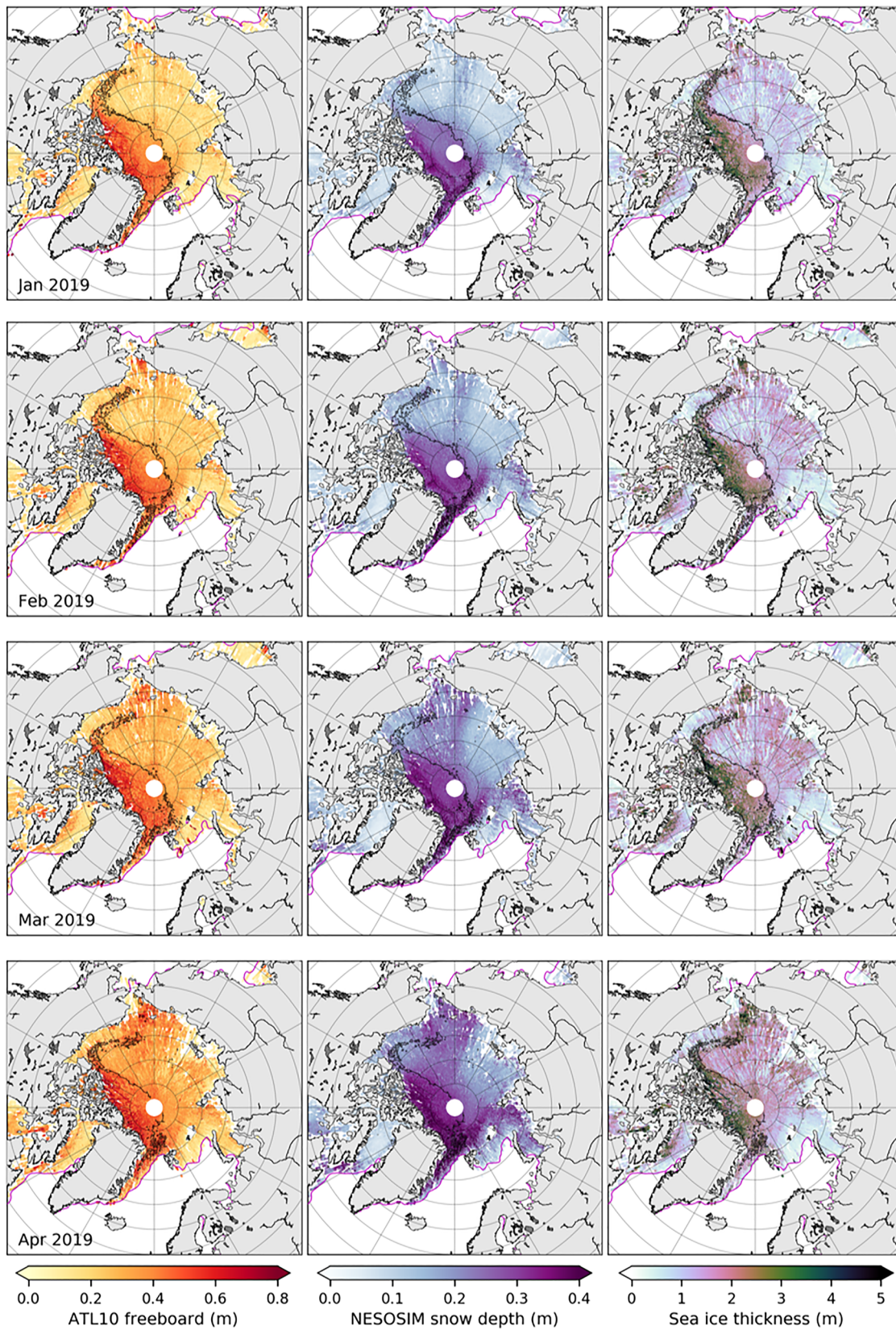
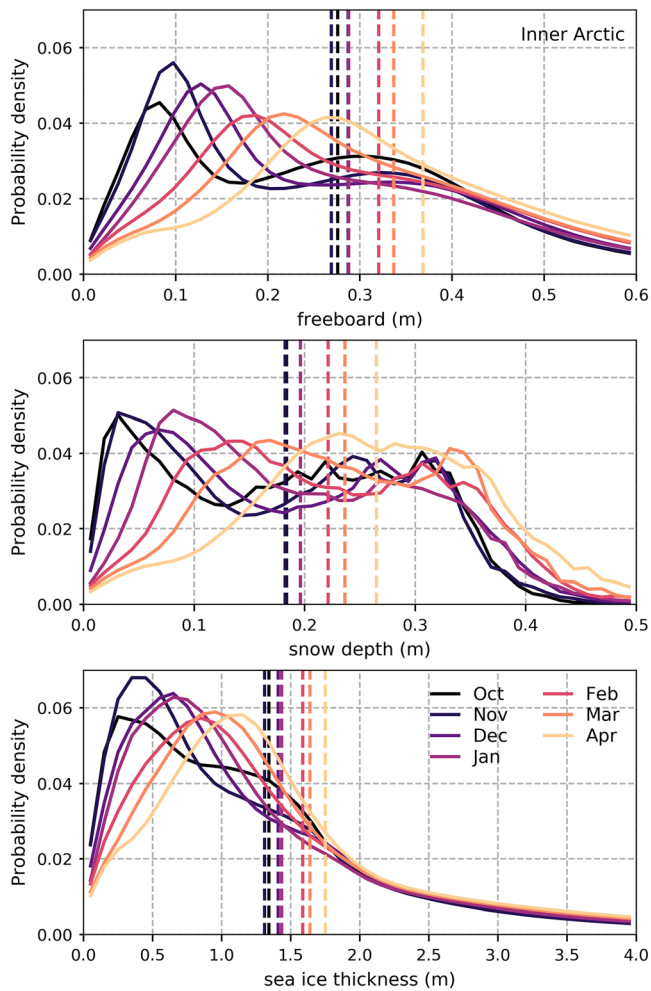


Figure 7. As in Figure 6 but for January (top row), February (second row), March (third row), and April (bottom row) 2019.



**Figure 8.** Monthly (October to April) histograms of the (top) freeboard, (middle) snow depth using the distributed NESOSIM snow loading ( $NS_{rd-pw}$ ), and (bottom) the resultant sea ice thickness within our Inner Arctic domain (Central Arctic, Beaufort, Chukchi, E. Siberian, and Laptev). The lines are plotted through the bin centers of the underlying histogram values using a bin width of 1.5, 1.25, and 10 cm, respectively, and are normalized and weighted using the individual segment lengths. The dashed lines show the mean monthly values for all data within this Inner Arctic domain.

(Arctic region maps given in Figure S5). We show results within this domain due to our higher confidence in the freeboards and snow loading compared to the more marginal Arctic seas. As discussed in section 3, the individual segment heights are weighted based on the individual segment lengths when producing these histograms. In this Inner Arctic domain, the ATL10 freeboards (just strong Beam 1) increase monotonically from 0.28 to 0.37 m (October to April), our NESOSIM snow depth increases from 0.18 to 0.26 m (October to April), and the derived ice thickness increases from  $\sim 1.34$  to 1.74 m (October to April). As shown in Kwok, Markus, Kurtz, et al. (2019), the freeboard distribution (using all the Arctic Ocean freeboard data) initially shows a bimodal distribution that evolves into a unimodal distribution by the end of winter, which we see in this more reduced Arctic domain also. This is thought to be driven by the negative feedback mechanism of sea ice growth (thinner FYI ice is less insulated so it grows faster through winter, e.g., Petty et al., 2018) that reduces the thickness difference between FYI and MYI through winter. Our (redistributed) NESOSIM snow depth distributions show a clearer bimodal distribution than freeboard, which become near unimodal by the end of winter. The thickness estimates exhibit a more unimodal distribution throughout winter.

The seasonal evolution of the regional ice thickness distributions across all eight of our Arctic study regions are shown in Figure 9. The predominantly MYI in the Central Arctic region is the thickest of all the regions, as expected, and shows a gradual monotonic increase in sea ice thickness from October through to April, with a mean increase of  $\sim 35$  cm ( $\sim 1.44$  m in October to  $\sim 1.80$  m in April). As in our Inner Arctic results, a slight bimodal distribution is observed in the October sea ice thickness distribution, which becomes clearly unimodal by December onwards. We see larger changes in the thickness distribution in the peripheral seas of the Eastern Arctic, as expected due to the more rapid ice growth of thinner FYI through the same negative ice growth feedback mechanism, with the Laptev, East Siberian, and Chukchi seas increasing monotonically from a mean of approximately 0.4–0.6 m in October to approximately 1.3–1.8 m in April, that is, a growth of  $\sim 1$  m through winter. The Barents and Kara seas show initial declines in the mean thickness, which appears to be due to the later freeze-up and appearance of FYI across the study region and the possible export of thicker ice from the region. The Beaufort Sea shows higher thickness than the other peripheral seas in October ( $\sim 1.2$  m) likely due to the inclusion of some thicker MYI (as evidenced from the maps in Figure 6), which increases to a thickness similar

to the other peripheral seas by April ( $\sim 1.65$  m). As discussed in section 2.1, we only use one of the strong beams (Beam 1) to produce these thickness estimates, but in Figure S6, we show the regional thickness distributions in January for each of the strong beams, highlighting the strong agreement between the beams in terms of the entire thickness distributions across all regions, with differences on the order of centimeters and mean differences of less than 10 cm.

Monthly ice thickness distributions delineated by ice type (FYI or MYI from the OSI SAF ice type product) are shown in Figure 10. Thickness distributions for all data collected across the Arctic are first shown in Figure 10a ( $\sim 1.35$  m in October to  $\sim 1.65$  m in April). Figures 10b and 10c show the clear differences in ice thickness distribution between ice type and, again, the stronger seasonal winter change in the FYI ice thickness distribution (a flattening/broadening of the distribution) compared to MYI, although the mean change in thickness between ice types is comparable. The MYI ice has a mean thickness of  $\sim 1.55$  m in October, which increases monotonically to  $\sim 2.3$  m in April. The FYI ice has a mean thickness of  $\sim 0.6$  m in October, which increases monotonically to  $\sim 1.4$  m in April. It is encouraging to note that our mean Arctic

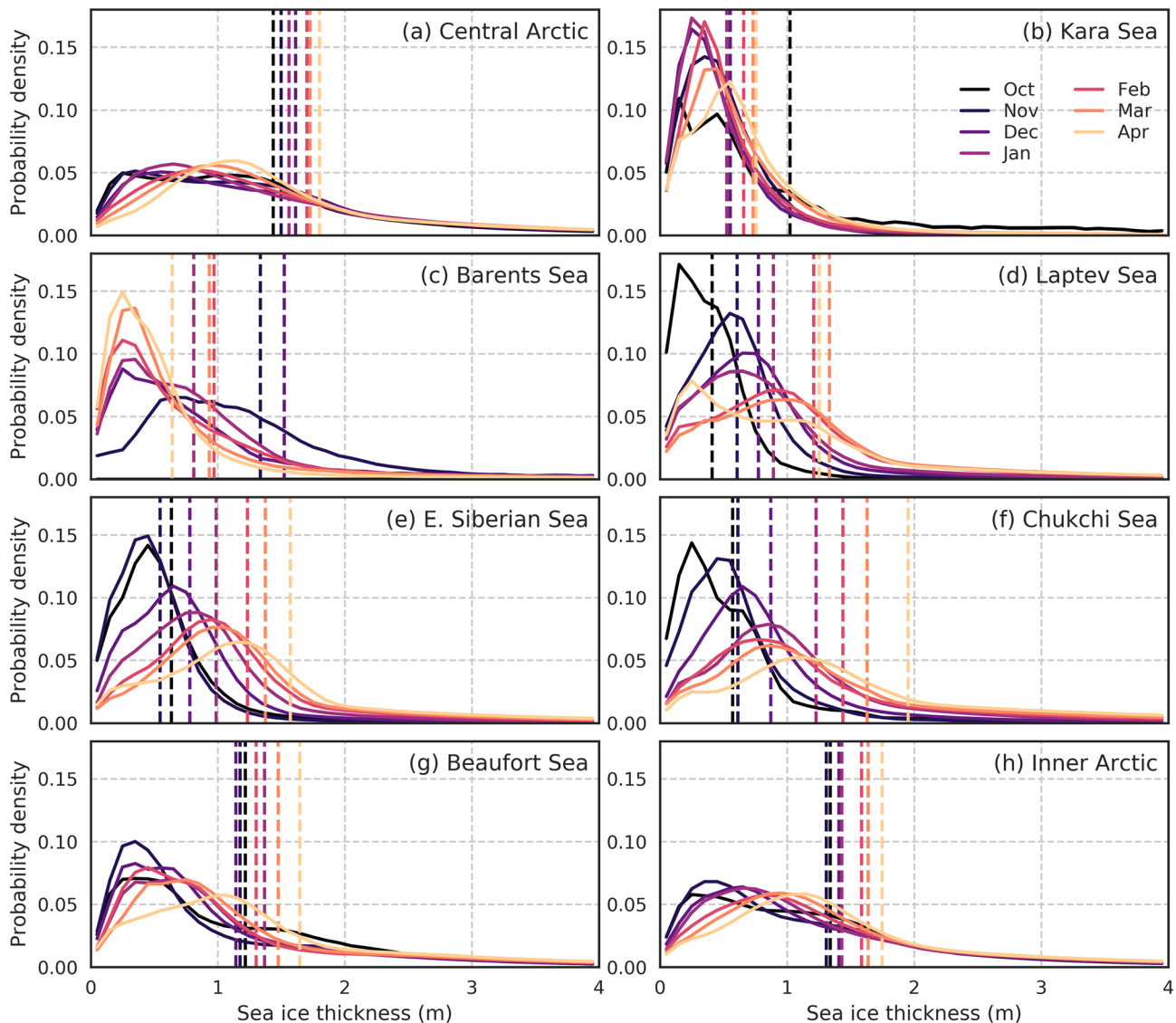


**Figure 9.** Monthly (October to April) histograms of the regional sea ice thickness estimated using the redistributed NESOSIM snow loading ( $NS_{rd-pw}$ ). The lines are plotted through the bin centers of the underlying histogram values using a bin width of 10 cm and are normalized and weighted using the individual thickness segment lengths in each month/region. The dashed lines show the mean monthly thickness values for all data found within each region.

FYI thickness increases through winter to a value similar to the MYI ice thickness at the start of our growth season.

#### 4.4. Gridded Sea Ice Thickness

To provide monthly gridded sea ice thickness estimates, we use a simple spatial binning approach, whereby we aggregate the along-track ice thickness data (and other variables included in the gridded data product) within a given bin/grid cell. We use the NSIDC  $25 \times 25$ -km polar stereographic grid ([https://nsidc.org/data/polar-stereo/ps\\_grids.html](https://nsidc.org/data/polar-stereo/ps_grids.html)) as this is a commonly used grid projection and enables easy comparisons with other data sets, such as passive microwave derived ice concentrations. We first produce gridded estimates of the daily data, weighting the estimates when binning based on the given segment lengths (as shown earlier in equation 2). Prior to this, we coarsen the raw along-track estimates using a 200-segment weighted mean to reduce the computational expense. We then produce monthly gridded estimates from these daily gridded data, again weighting these based on the mean segment length in a given daily grid cell. Because of data gaps caused by the orbit cycles, we use a simple inverse distance weight scheme to interpolate

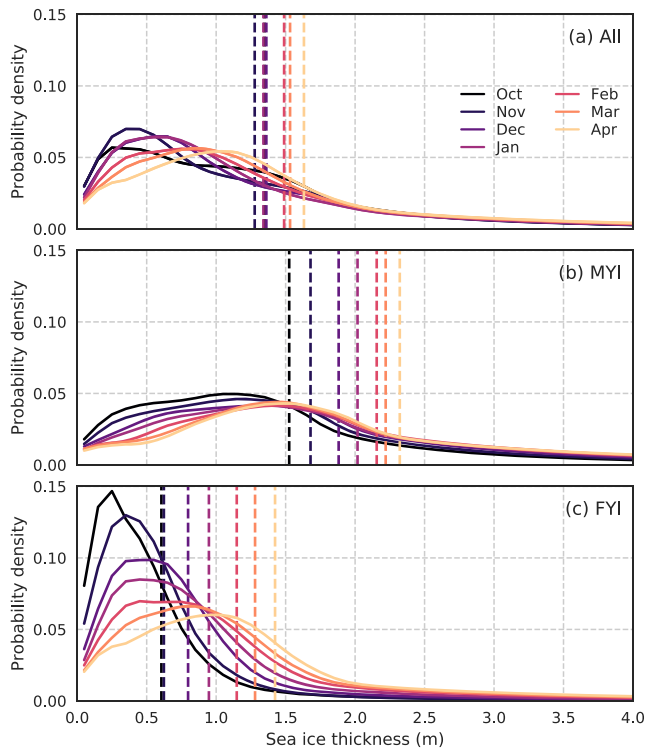


**Figure 10.** Monthly (October to April) histograms of the sea ice thickness delineated by ice type (top: all ice types, middle: multiyear ice, and bottom: first-year ice), estimated using the distributed NESOSIM snow loading ( $NS_{rd-pw}$ ). The lines are plotted through the bin centers of the underlying histogram values using a bin width of 10 cm and are normalized and weighted using the individual thickness segment lengths in each month/ice type. The dashed lines show the mean monthly thickness values for all data within each ice-type delineation.

between grid cells (only for missing data within two grid cells of a valid grid cell in four directions). We choose to produce a monthly gridded thickness estimate for all grid cells with at least 1 day of data but also provide the number of days of valid binned data in the product to enable stricter masking based on user needs. Another factor to consider when using the binned data is the influence of the orbit cycle on the effective date of the data contained within a given bin, which shows a spatial pattern that oscillates as a function of longitude between the start and end of the month (shown in Figure S7). We have not attempted to account for this in this initial analysis and data product release but will explore possible corrections in future efforts (e.g., applying a simple thermodynamic model to correct toward the middle day of the month or a simple spatial smoothing). The presence of optically thick clouds can also hinder freeboard retrievals and change the spatial sampling within a given month.

The gridded November 2018 to April 2019 monthly sea ice thickness estimates are shown in Figure 11, with the monthly thickness changes given in Figure 12. The thickness maps agree well with the thickness data displayed earlier using the high-resolution along-track data (Figures 6 and 7) but without some of the small data gaps due to our limited spatial interpolation procedure. The monthly thickness changes are predominantly positive, as expected, with the spatial inhomogeneity in these fields likely due to a combination of both physical (e.g., variable ice dynamics) and unphysical (spatial sampling differences across months) effects. We also show our estimate of the monthly systematic ice thickness uncertainty in Figure 13, as introduced in section 3.2 (we assume that the random errors are reduced to 0 at this 25-km scale). These absolute systematic uncertainties show a regional pattern similar to the gridded thickness data (higher uncertainties along the Greenland/Canadian Arctic coastline) but also high uncertainties in Fram Strait and the Barents/Kara sector where our knowledge of snow is highly uncertain. The uncertainties expressed as a percentage of the monthly thickness show high values generally in the thinner peripheral seas of the Arctic, and especially the Kara sea in November–January.

#### 4.5. Comparisons With CryoSat-2

We compare our monthly sea ice thickness estimates with four different CryoSat-2 data products (CPOM, AWI, GSFC, and JPL). We regrid the monthly gridded CS-2 estimates to the NSIDC  $25 \times 25$ -km polar stereographic grid using a simple nearest neighbor interpolation scheme and compare these with our gridded IS-2 thickness estimates that have been produced using the same snow loading and ice density assumptions as the given CS-2 product, as summarized in Table 2. We mask all data below 0.25 m and outside of our Inner Arctic domain due to the questionable validity of the W99 snow loading in the more marginal seas and also because of the known issues of CS-2 capturing these thinner ice regimes (e.g., Ricker et al., 2017). It is worth noting that all the products employ different assumptions regarding data quality (e.g., filtering) and spatial interpolation/smoothing, so this analysis should be viewed as a simple product comparison rather than a complete assessment of differences between the retrievals.

Figure 14 shows the ice thickness comparisons (using the same CS-2 input assumptions) in November. The full November through April comparison statistics of correlation coefficient ( $r$ ), mean thickness bias (MB), and standard deviation (SD, after bias correcting) are summarized in Table 2. The April 2019 thickness comparisons are shown in Figure S8. The November IS-2/C-2 thickness maps show good agreement in the spatial distribution of ice thickness, although the area of thickest ice along the Greenland/Canadian Arctic coastline appears to extend further north in the CS-2 estimates, across all the products. This difference contributes a consistent mean bias between the IS-2 and CS-2 products across all months (IS-2 consistently thinner than CS-2), with the bias ranging from 0.33 (JPL) to

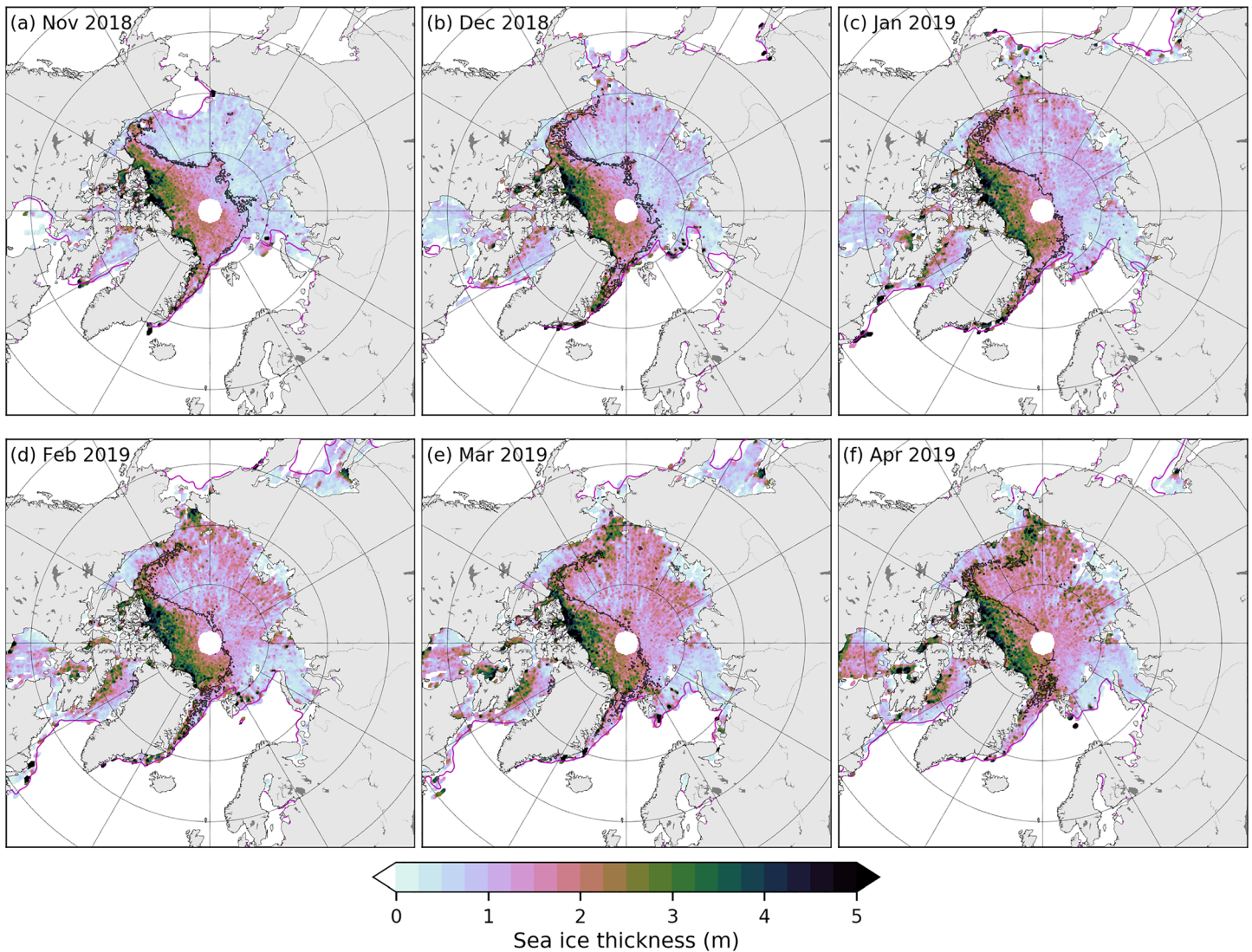


**Figure 11.** Monthly mean (November to April) winter gridded sea ice thickness from ICESat-2 ( $NS_{rd-pw}$  input assumptions). The magenta line is the 50% ice concentration contour from the CDR passive microwave data set, and the black line shows the first-year ice/multiyear ice boundary from the OSI SAF ice-type product.

0.69 m (GSFC). These biases represent a significant fraction of the mean basin-scale ice thicknesses described earlier (~1.3 to 1.7 m). The November correlations are generally strong ( $r = 0.67$  to  $0.77$ ) due to the good agreement in the regional ice thickness distribution across the Arctic, and the standard deviations are largely consistent across the CS-2 products ( $SD = 0.59$  to  $0.78$  m). The correlations are similar in December ( $r = 0.65$  to  $0.73$ ) but weaken from January through to April ( $r = 0.19$  to  $0.53$  in April). The mean biases decrease through winter ( $MB = 0.06$  to  $0.34$  m in April); however, the standard deviation increases ( $SD = 0.97$  to  $1.07$  m in April) as the thickness biases become less regionally consistent. The CPOM comparisons generally show the lowest SDs of all the products, although the difference is small. It is worth noting that the JPL product has the lowest biases of all the products but also has the most missing data of all the products, especially within the thicker MYI zone.

We also show in Table 2 the statistical comparisons using the four monthly CS-2 products and the primary IS-2 product presented here based on the redistributed NESOSIM data ( $NS_{rd-pw}$ ). We provide this to show the correspondence between our “best guess” ice thickness estimate and the various CS-2 products, despite the use of different input assumptions. The agreements between CS-2 and IS-2 are often better than the

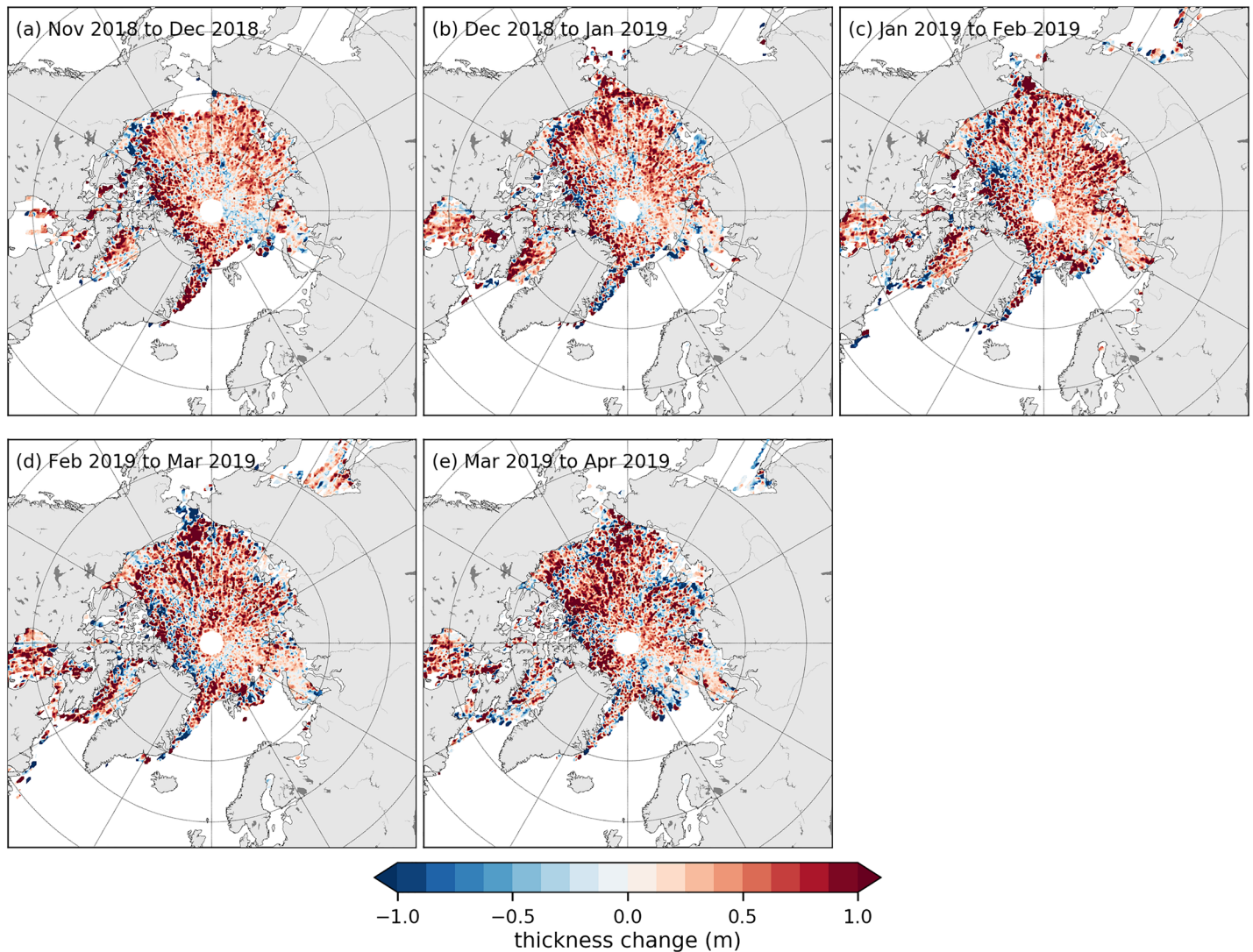


**Figure 12.** Monthly mean change (e.g., November to December) in the gridded monthly sea ice thickness from ICESat-2 ( $NS_{rd-pw}$  input assumptions).

comparisons using the same input assumptions, especially with respect to the correlation coefficient in the AWI and GSFC CS-2 data and the CPOM and JPL data from January onwards.

#### 4.6. Comparisons With ICESat

To place these results in a longer-term context, we show comparisons of our end of winter Arctic ice thickness with end of winter ice thickness obtained from ICESat freeboards (described in section 2.5). As the ICESat data were obtained in approximately 2-month campaign cycles, we compare our mean February/March 2019 gridded thickness estimates with the February/March 2008 (19 February–21 March 2018, FM08)—the final ICESat campaign. We also show the previous FM ICESat campaign years (FM03, FM04, FM05, and FM06) to provide a longer-term context. Note again that we use the same snow loading, sea ice density, and snow redistribution ( $NS_{rd-pw}$ , Table 2) to generate these updated ICESat thickness estimates. We constrain the thickness estimates in this comparison to our Inner Arctic domain (Central Arctic, Beaufort, Laptev, and East Siberian seas; Figure S5) to focus on thickness declines instead of extent/volume, as the more peripheral seas have experienced a well reported decline in winter Arctic sea ice extent in recent years (e.g., Petty et al., 2018), which is not a focus of this study. The thickness comparisons are shown in Figure 15, which demonstrate a continued thinning and loss of ice in this 11-year period (since the end of ICESat). The spatial maps highlight mainly thinning across the Arctic Ocean except for small increases to the northeast of Greenland, within the Beaufort Sea and the southern Chukchi Sea. The

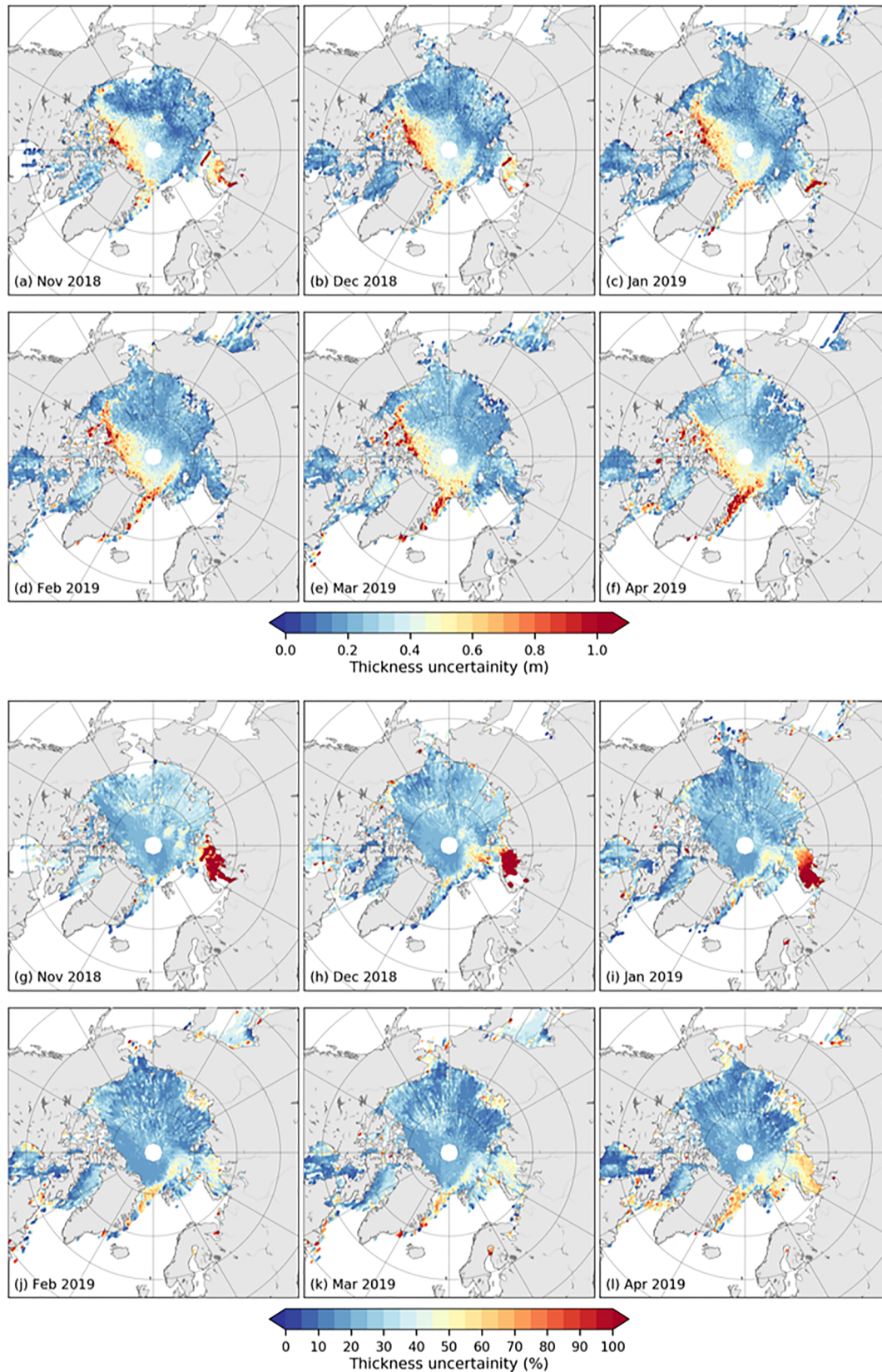


**Figure 13.** (a–f) Monthly mean (November to April) systematic sea ice thickness uncertainty estimate and (g–l) expressed as a percentage of the mean thickness of the given month.

**Table 2**  
Statistics of the ICESat-2/CryoSat-2 Monthly Gridded Thickness Comparisons

		November	December	January	February	March	April
Correlation coefficient (r)	GSFC	0.67 ( <b>0.71</b> )	0.69 ( <b>0.71</b> )	0.58 ( <b>0.65</b> )	0.44 ( <b>0.54</b> )	0.38 ( <b>0.53</b> )	0.29 ( <b>0.46</b> )
	JPL	<b>0.69</b> (0.71)	0.73 (0.71)	0.63 ( <b>0.62</b> )	0.54 ( <b>0.61</b> )	0.48 ( <b>0.49</b> )	0.35 ( <b>0.44</b> )
	CPOM	<b>0.77</b> (0.73)	<b>0.72</b> (0.73)	0.64 ( <b>0.70</b> )	0.51 ( <b>0.61</b> )	0.43 ( <b>0.63</b> )	0.53 ( <b>0.58</b> )
	AWI	0.68 ( <b>0.76</b> )	0.65 ( <b>0.72</b> )	0.52 ( <b>0.67</b> )	0.41 ( <b>0.65</b> )	0.30 ( <b>0.60</b> )	0.19 ( <b>0.48</b> )
Mean bias (m)	GSFC	0.69 ( <b>0.69</b> )	0.70 ( <b>0.69</b> )	0.51 ( <b>0.42</b> )	<b>0.41</b> (0.48)	<b>0.32</b> (0.51)	<b>0.06</b> (0.47)
	JPL	0.33 ( <b>0.30</b> )	0.31 ( <b>0.31</b> )	0.30 ( <b>0.30</b> )	<b>0.24</b> (0.42)	<b>0.21</b> (0.52)	<b>0.09</b> (0.52)
	CPOM	0.62 ( <b>0.43</b> )	0.51 ( <b>0.40</b> )	0.51 ( <b>0.36</b> )	0.47 ( <b>0.45</b> )	<b>0.55</b> (0.66)	<b>0.34</b> (0.65)
	AWI	0.67 ( <b>0.40</b> )	0.51 ( <b>0.31</b> )	0.42 ( <b>0.31</b> )	0.43 ( <b>0.41</b> )	<b>0.48</b> (0.60)	<b>0.30</b> (0.58)
Standard deviation (m)	GSFC	0.76 ( <b>0.73</b> )	0.74 ( <b>0.69</b> )	0.76 ( <b>0.69</b> )	0.88 ( <b>0.79</b> )	0.86 ( <b>0.75</b> )	1.04 ( <b>0.88</b> )
	JPL	0.74 ( <b>0.70</b> )	0.66 (0.66)	0.70 ( <b>0.69</b> )	0.80 ( <b>0.73</b> )	0.88 ( <b>0.77</b> )	1.01 ( <b>0.91</b> )
	CPOM	<b>0.59</b> (0.67)	<b>0.55</b> (0.63)	<b>0.57</b> (0.61)	0.70 (0.70)	0.78 ( <b>0.68</b> )	0.97 ( <b>0.84</b> )
	AWI	0.78 ( <b>0.70</b> )	0.73 ( <b>0.66</b> )	0.74 ( <b>0.66</b> )	0.87 ( <b>0.73</b> )	0.89 ( <b>0.75</b> )	1.07 ( <b>0.88</b> )

Note. The values in brackets are the comparisons using the IS-2 NS<sub>rd-pw</sub> product instead of the CS-2 input assumptions. Bold denotes which comparison provides the best statistical agreement in the relevant metric.

Beaufort/Chukchi increase appears to be the result of a typical anticyclonic Beaufort Gyre circulation exporting thicker ice from the Central Arctic into the region this past winter. Averaged across the entire Inner Arctic domain, we estimate a thinning of  $\sim 0.37$  m or  $\sim 20\%$  of the February/March 2008 ICESat thickness. Figure 15 demonstrates that the FM08 campaign was the thinnest of all the FM ICESat campaign periods, and the ICESat to ICESat-2 thickness decline is clearly outside of the range of ICESat interannual thickness variability. Our results suggest a 0.75-m thinning over the approximately 5-year ICESat period (2003–2008), similar to the  $\sim 0.5$ -m decrease reported in Kwok et al. (2009) within a similar Inner Arctic domain, with this thinning occurring mainly within the MYI regime. Our results suggest that the overall thinning has continued and appears to still be occurring mainly within the MYI regime. The possible low bias in our IS-2 thickness estimates compared to CS-2 means these results should be treated with caution until a more complete validation has been carried out.

## 5. Summary and Outlook

In this study, we presented our new processing chain for converting the official along-track ICESat-2 sea ice freeboard product (ATL10) into sea ice thickness for all profiles collected during the Arctic winter of 2018/2019 (15 October–30 April). The thicknesses are calculated assuming hydrostatic equilibrium and assumptions of snow depth/density and sea ice density, primarily utilizing daily snow depth and density estimates from NESOSIM forced by ERA-Interim snowfall. We use just one of the strong beams (strong Beam 1) in this initial effort but shows good consistency across the strong beams in terms of our regional thickness distributions. The coarse resolution (100 km) snow depths were redistributed onto the high-resolution but variable resolution ( $\sim 30$ – $100$  m) ATL10 data using a linear piecewise function based on an analysis of snow depth and freeboard data collected by NASA's Operation IceBridge mission. We provide estimates of the ice thickness uncertainty by combining estimates of random uncertainty and systematic uncertainty driven by our various input assumptions (including a modified version of the Warren snow depth climatology).

We present regional and ice type sea ice thickness distributions and highlight their seasonal evolution through the first winter season (November to April) of ICESat-2 data collection. Segment weighting the data is an important step when producing such statistical analyses. We demonstrate the generation of a gridded thickness product using a simple binning procedure and compare this with gridded estimates of sea ice thickness from ESA's CryoSat-2 (CS-2) satellite mission using the same input assumptions as the various CS-2 products. The comparisons show moderate/strong correlations but significant biases of up to several tens of centimeters depending on the month or CS-2 product analyzed. The agreement tends to reduce through the winter season for all the CS-2 products, which corresponds with the reduced regional gradient across the Arctic in April compared to October. The comparisons are generally better when the CS-2 products are compared against the IS-2 NS<sub>rd-pw</sub> product rather than the IS-2 thickness estimates produced

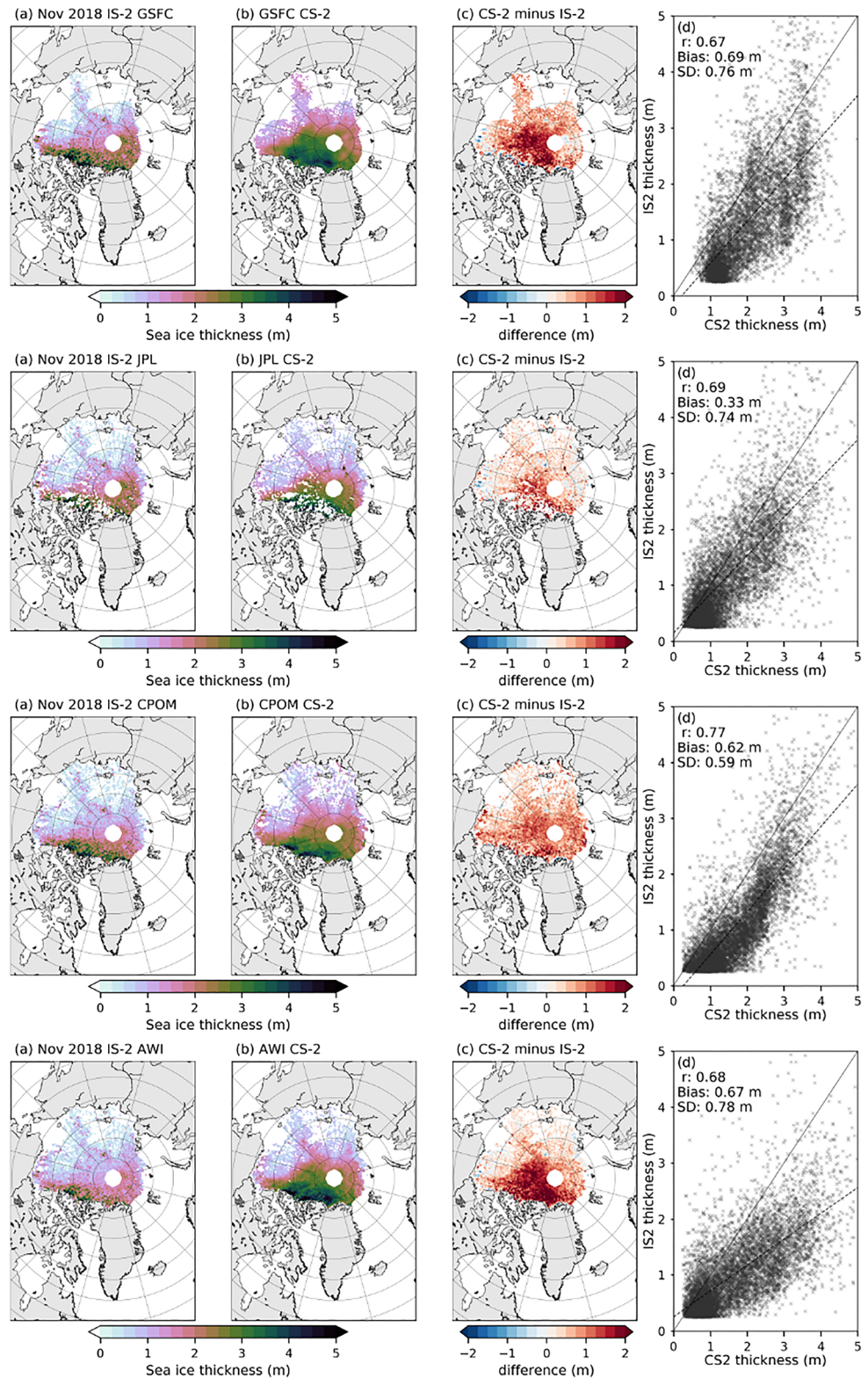


**Figure 14.** Comparisons of the gridded November 2018 IS2 thickness data with NASA GSFC (top) JPL (second row), CPOM (third row), and AWI (bottom row) CS-2 sea ice thickness data. The IS-2 thickness data have been processed with the respective CS-2 product input assumptions (Table 1). All data less than 0.25 m and outside of an Inner Arctic domain have been masked. The solid line in the scatter plots shows the 1:1 reference, and the dashed line shows the linear regression.

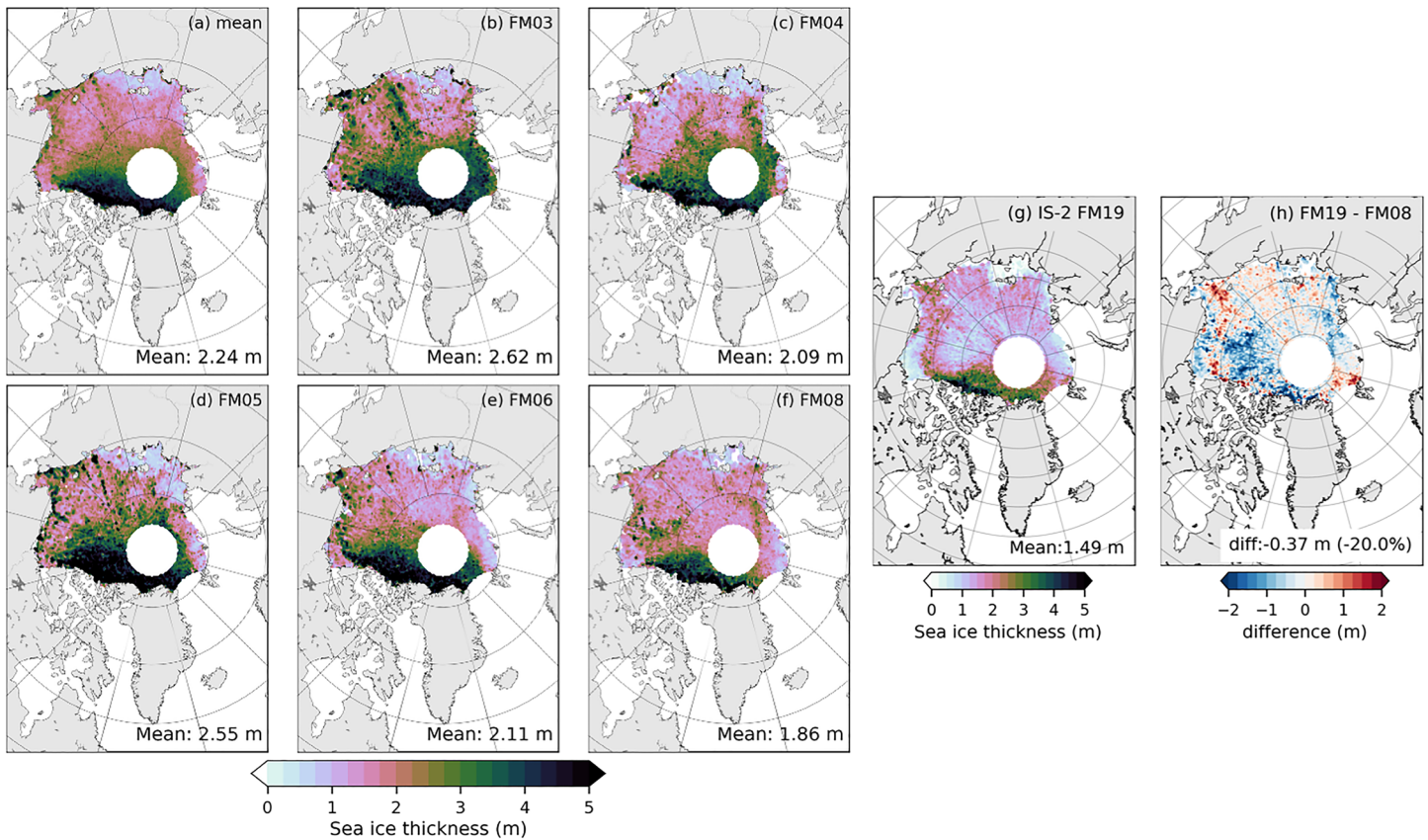


**Figure 15.** Comparisons of the (a) gridded mean FM08 (19 February–21 March 2008) ICESat thickness data and (b) February/March 2019 mean ICESat-2 data. Data outside of our Inner Arctic domain have been masked in this comparison. The ICESat-2 minus ICESat difference is shown in panel (c) with this difference expressed as a percentage of the ICESat FM08 data in panel (d).

using the same CS-2 input assumptions. In all cases, the IS-2 thicknesses generated are thinner than the CS-2 products.

Comparisons of our February/March 2019 thickness estimates with ICESat February/March 2008 ice thickness estimates, the latest and thinnest of the February/March ICESat period, suggest an  $\sim 0.37$  m or  $\sim 20\%$  thinning within our Inner Arctic domain in this 11-year time period. In both the CS-2 and ICESat comparisons, more work is needed to understand possible biases in the IS-2 data to increase our confidence in these findings.

### 5.1. Understanding the Thickness Differences Between ICESat-2 and CryoSat-2

A potential cause of these thickness biases between IS-2 and CS-2 is a systematic bias in either the IS-2 or CS-2 freeboards. Note again that CS-2 is expected to provide an estimate of the ice freeboard (not including the overlying snow cover), while IS-2 provides total (ice plus snow) freeboard. As CS-2 data have been well validated against various independent datasets, arguably the most obvious explanation is a low bias in the ATL10 freeboards. This could be caused by erroneous surface classification (thin ice being incorrectly classified as leads) or the sensor failing to capture high surface features. Another possible explanation is that the CS-2 freeboards are biased high. This could be due to the radar penetration depth being higher than the assumed ice-snow interface, a known issue with CS-2 especially in wet snow conditions (e.g., King et al., 2018; Nandan et al., 2017; Willatt et al., 2011). Additionally, this could be caused by erroneous surface classification, off-nadir reflections, or the CS-2 radar being overly sensitive to high surface topography features.

Another possible issue is the removal of snow in laser altimetry for low freeboards/high snow depths. In the case of laser profiling, the snow depth is reduced when a total freeboard is measured higher than the input snow depth assumption to prevent a negative ice freeboard. In radar profiling, snow is never removed and

can instead pile up on the inferred ice (not total) freeboard, increasing thickness compared to the laser measurement. Thus, despite using the same snow loading assumptions, they are applied differently in the thickness conversion equation. Errors in the assumed snow depth could also cause a divergence in the thickness estimates due to the different calculation of thickness from radar and laser profiling (see, e.g., Giles et al., 2007). As an example, for an ice floe with a total freeboard of ~35 cm and snow depth of ~15 cm, falsely assume a snow loading of 20 cm would produce a thickness of ~2 m for laser and ~2.5 m for radar profiling (the actual thickness should be ~2.3 m), even if both measured the relevant (ice or total) freeboards correctly. Providing more accurate snow depths can mitigate these last two issues, especially the latter (note again that we used the same version of the modified W99 climatology in our CS-2 comparisons). The better agreements, mainly in terms of the correlation coefficient, between CS-2 and the IS-2 data using our primary  $N_{rd-pw}$  thickness product (i.e., using different input assumptions) are noteworthy and allude to possible issues with the underlying input assumptions in the CS-2 thickness products, although this was not sufficient to remove the bias. Figures S2–S4 show the difference between the NESOSIM and W99m5 data, which can be high in certain regions; however, it remains challenging to fully validate either. Both were shown to exhibit no obvious bias when compared with OIB data (Petty, Webster, et al., 2018), while recent (2017) in situ snow and ice data collected from the Lincoln Sea toward North Pole showed similar (30–40 cm) April snow depth distributions to those shown in both products (Haas et al., 2017). More field campaigns like this (covering large expanses of the ice pack) are needed across different locations and times of the year to get a better sense of basin-scale snow biases.

Finally, it is also worth recognizing that the satellites have different orbit cycles and thus represent different profiles across the Arctic Ocean, although the relatively high monthly coverage in both products should mitigate this possible issue. Joint comparisons against independent thickness data, for example, from the spring 2019 Operation IceBridge campaign, AWI's spring 2019 IceBird campaign (Haas et al., 2010), and the Beaufort Gyre Exploration Project upward looking sonar moorings (Krishfield et al., 2014), will be invaluable in future efforts to understand and hopefully reconcile these biases.

## 5.2. Toward an ICESat-2 Sea Ice Thickness Product

As stated in the Section 1, much of this study was motivated by the community need for routine estimates of basin-scale sea ice thickness, which are not being directly provided by ICESat-2. As such, we plan to provide routine along-track and gridded sea ice thickness data sets shortly after the public release of ATL10 data. The along-track thickness product includes the various sea ice thickness estimates, ancillary data, and individual (random and systematic) uncertainty estimates to enable more comprehensive evaluation for the more advanced user. The gridded product contains only the sea ice thickness derived using the piecewise redistributed NESOSIM data ( $N_{rd-pw}$ ), along with core variables including freeboard, NESOSIM ( $N_{rd-pw}$ ) snow depth/density, OSI SAF ice type, mean day of month, number of valid days of data in each bin, and the total thickness uncertainty (just the mean systematic uncertainty at this scale), with the output for April 2019 given in Figure S7. The current latency of ATL10 data availability is ~45 days after a given IS-2 orbit pass, and we hope to provide the thickness data within days of this release. We currently use ERA-Interim snowfall to force the NESOSIM model, which has an approximately 2-month data latency; however, ERA Interim is being replaced by ERA5, which has a data latency of only ~2 days, similar to the CDR ice concentration (Meier et al., 2017) and OSI-SAF ice drift (Lavergne et al., 2010) product latencies that are also needed to produce NESOSIM snow depths. ERA5 exhibits a high bias in snowfall compared to ERA-I (Cabaj et al., 2020; Wang et al., 2019), so updated ERA5/NESOSIM model calibration is currently ongoing in preparation for the 2019/2020 winter. Both the NESOSIM and ICESat-2 source codes are open source and publicly available (links provided below).

## 5.3. Future Work

Future work will focus on the validation of these ice thickness estimates and providing better constraints on our uncertainty estimates. A more detailed comparison of the freeboards generated by CryoSat-2 is needed, while efforts are ongoing to directly produce basin-scale thickness estimates from the expected difference in IS-2 and CS-2 freeboards (as the CryoSat-2 radar penetrates down toward the snow-ice interface the difference could provide some measure of snow depth). We also hope to analyze data from satellite imagery to provide a more detailed assessment of the surface classification procedure in ATL10 and to ensure the freeboards of thin/new ice are being captured correctly. Dedicated airborne campaigns (e.g., NASA's

Operation IceBridge and AWI's IceBird) will be used to provide direct validation of the freeboard and thickness variability along direct underflights, while data collected by the Beaufort Gyre Exploration Project moorings will provide coincident draft measurements that can be compared with the freeboards and thickness using coincident input conversion assumptions. Data from upcoming field programs (e.g., the Multidisciplinary drifting Observatory for the Study of Arctic Climate) could provide valuable validation of the freeboards and surface classifications in ATL10 and our snow loading and sea ice density assumptions.

We also intend to extend these estimates across all seasons. To do this requires improved knowledge of the surface classification procedure in spring/summer, when surface melt will make differentiating melt ponds from leads a challenge (erroneously classifying melt ponds as leads will bias the freeboard and thickness estimates low). The Warren snow depth/density climatology provides the only known estimates of summer snow conditions, so more needs to be done to extend the snow depth and density modeling efforts through the melt season, as discussed in Petty, Webster, et al. (2018). Estimates of Antarctic sea ice thickness remain elusive as we are generally hindered by the lack of basin-scale snow information currently available. Previous ICESat analyses (e.g., Kurtz & Markus, 2012) proceeded by assuming that the snow ice interface was at sea level (all the freeboard is snow) based on ship-based observations of the ice cover. However, more recent analysis of NASA's Operation IceBridge aerial surveys in the Weddell and Bellingshausen seas has questioned this assumption (Kwok & Kacimi, 2018; Kwok & Maksym, 2014; Petty et al., 2017). More sophisticated snow modeling efforts, combined with these new airborne data sets, are urgently needed.

#### Data Availability Statement

The along-track and gridded sea ice thickness estimates produced in this study are available through the National Snow and Ice Data Center (NSIDC) at <https://doi.org/10.5067/JTI5YG3S6VAJ> and <https://doi.org/10.5067/CV6JEXEE31HF> respectively. The data include the key input data and uncertainties as explained in more detail in the data portals. The gridded thickness data repository also includes the gridded ICESat thickness data presented in this study.

The ICESat-2 ATL10 sea ice freeboard data (designated Release 002) can be obtained from the NSIDC (<https://nsidc.org/data/atl10>). Daily and monthly NASA Climate Data Record (CDR) version 3 ice concentration data were obtained from the NSIDC (<https://nsidc.org/data/G02202>). The ERA-Interim snowfall and wind data were obtained through the ECMWF Meteorological Archival and Retrieval System ([http://apps.ecmwf.int/datasets/data/interim\\_full\\_daily/](http://apps.ecmwf.int/datasets/data/interim_full_daily/), last access: 15 August 2019). The EUMETSAT OSI SAF ice motion data were obtained through their own web portal (<http://osisaf.met.no/p/ice/>, last access: 1 May 2019). The OSI SAF ice type data were obtained from their ftp repository (<ftp://osisaf.met.no/prod/ice/type/>). The NASA GSFC CryoSat-2 (CS-2) Arctic sea ice thickness data were obtained from the NSIDC (<https://nsidc.org/data/RDEFT4>, last access: 1 May 2019). The CPOM CS-2 thickness data were obtained from their web portal (<http://www.cpom.ucl.ac.uk/csopr/seaice.html>, last access: 1 May 2019). The AWI CS-2 thickness data were obtained from their web portal ([http://data.seaiceportal.de/data/cryosat2/version2.1/l3c\\_grid](http://data.seaiceportal.de/data/cryosat2/version2.1/l3c_grid), last access: 1 May 2019). The NASA JPL CS-2 thickness data are available from Dr. Ron Kwok upon request.

#### Code Availability

The entire processing code is written in the open source language Python and is publicly available on GitHub (<https://github.com/akpetty/ICESat-2-sea-ice-thickness>). We hope this will enable community involvement in expected developments of this ICESat-2 sea ice thickness product. The repository also includes example analysis/plotting scripts used in this study.

#### Acknowledgments

We would like to thank the entire ICESat-2 engineering and science teams for all their efforts in preparing for the launch of ICESat-2 and ongoing work in maintaining the satellite and generating these highly valuable data products. Thanks to Al Ivanoff for processing and sharing rapid and preliminary versions of the ATL10 freeboard product to enable early assessments of these data. Thanks also to CPOM for providing their monthly region mean Warren snow depth/density estimates.

#### References

- Aagaard, K., & Carmack, E. C. (1989). The role of sea ice and other fresh water in the Arctic circulation. *Journal of Geophysical Research*, *94*(C10), 14,485–14,498. <https://doi.org/10.1029/JC094iC10p14485>
- Alexandrov, V., Sandven, S., Wahlin, J., & Johannessen, O. M. (2010). The relation between sea ice thickness and freeboard in the Arctic. *The Cryosphere*, *4*(3), 373–380. <https://doi.org/10.5194/tc-4-373-2010>
- Allard, R. A., Farrell, S. L., Hebert, D. A., Johnston, W. F., Li, L., Kurtz, N. T., et al. (2018). Utilizing CryoSat-2 sea ice thickness to initialize a coupled ice-ocean modeling system. *Advances in Space Research*, *62*(6), 1265–1280. <https://doi.org/10.1016/j.asr.2017.12.030>

- Blockley, E. W., & Peterson, K. A. (2018). Improving Met Office seasonal predictions of Arctic sea ice using assimilation of CryoSat-2 thickness. *The Cryosphere*, *12*(11), 3419–3438. <https://doi.org/10.5194/tc-12-3419-2018>
- Breivik, L. A., Eastwood, S., & Lavergne, T. (2012). Use of C-band scatterometer for sea ice edge identification. *IEEE Transactions on Geoscience and Remote Sensing*, *50*(7), 2669–2677. <https://doi.org/10.1109/TGRS.2012.2188898>
- Bunzel, F., Notz, D., & Pedersen, L. T. (2018). Retrievals of Arctic sea-ice volume and its trend significantly affected by interannual snow variability. *Geophysical Research Letters*, *45*, 11,751–11,759. <https://doi.org/10.1029/2018GL078867>
- Cabaj, A., Kushner, P. J., Fletcher, C. G., Howell, S., & Petty, A. A. (2020). Constraining reanalysis snowfall over the Arctic Ocean using CloudSat observations. *Geophysical Research Letters*, *47*. <https://doi.org/10.1029/2019GL086426>
- Carmack, E. C., Yamamoto-Kawai, M., Haine, T. W. N., Bacon, S., Bluhm, B. A., Lique, C., et al. (2016). Freshwater and its role in the Arctic marine system: Sources, disposition, storage, export, and physical and biogeochemical consequences in the Arctic and global oceans. *Journal of Geophysical Research: Biogeosciences*, *121*, 675–717. <https://doi.org/10.1002/2015JG003140>
- Cavalieri, D., & Markus, T. (2003). EOS Aqua AMSR-E Arctic sea ice validation program: Arctic2003 aircraft campaign flight report. *NASA/TM-2006-214142, atl. Aeronaut. and Space Admin., Washington, D. C.*, 27.
- Cavalieri, D., Parkinson, C., Gloersen, P., & Zwally, J. H. (1996). Sea ice concentrations from Nimbus-7 SMMR and DMSP SSM/I-SSMIS passive microwave data, Version 1. [January 2003–December 2008]. Boulder, Colorado USA: NASA DAAC at the National Snow and Ice Data Center. <https://doi.org/10.5067/8GQ8LZQVLOVL>
- Comiso, J. C. (2000). Bootstrap sea ice concentrations from Nimbus-7 SMMR and DMSP SSM/I-SSMIS. Version 2. [January 2000–December 2010]. Boulder, Colorado USA: NASA DAAC at the National Snow and Ice Data Center. <https://doi.org/10.5067/J6JQLS9EJ5HU>
- Comiso, J. C., Cavalieri, D. J., Parkinson, C. L., & Gloersen, P. (1997). Passive microwave algorithms for sea ice concentration: A comparison of two techniques. *Remote Sensing of Environment*, *60*(3), 357–384. [https://doi.org/10.1016/S0034-4257\(96\)00220-9](https://doi.org/10.1016/S0034-4257(96)00220-9)
- Dee, D. P., Uppala, S. M., Simmons, A. J., Berrisford, P., Poli, P., Kobayashi, S., et al. (2011). The ERA-interim reanalysis: Configuration and performance of the data assimilation system. *Quarterly Journal of the Royal Meteorological Society*, *137*(656), 553–597. <https://doi.org/10.1002/qj.828>
- Doble, M. J., Skourup, H., Wadhams, P., & Geiger, C. A. (2011). The relation between Arctic sea ice surface elevation and draft: A case study using coincident AUV sonar and airborne scanning laser. *Journal of Geophysical Research*, *116*, C00E03. <https://doi.org/10.1029/2011JC007076>
- Fetterer, F., Savoie, M., Helfrich, S., & Clemente-Colón, P. (2010). Multisensor Analyzed Sea Ice Extent-Northern Hemisphere (MASIE-NH), Version 1. Boulder, Colorado USA. NSIDC: National Snow and Ice Data Center. [doi:https://doi.org/10.7265/N5GT5K3K](https://doi.org/10.7265/N5GT5K3K)
- Giles, K. A., Laxon, S. W., Wingham, D. J., Wallis, D. W., Krabill, W. B., Leuschen, C. J., et al. (2007). Combined airborne laser and radar altimeter measurements over the Fram Strait in May 2002. *Remote Sensing of Environment*, *111*(2-3), 182–194. <https://doi.org/10.1016/j.rse.2007.02.037>
- Haas, C., Beckers, J., King, J., Silis, A., Stroeve, J., Wilkinson, J., et al. (2017). Ice and snow thickness variability and change in the high Arctic Ocean observed by in situ measurements. *Geophysical Research Letters*, *44*, 10,462–10,469. <https://doi.org/10.1002/2017GL075434>
- Haas, C., Hendricks, S., Eicken, H., & Herber, A. (2010). Synoptic airborne thickness surveys reveal state of Arctic sea ice cover. *Geophysical Research Letters*, *37*, L09501. <https://doi.org/10.1029/2010GL042652>
- Hendricks, S., & Ricker, R. (2016). User guide—AWI CryoSat-2 sea ice thickness data product (v1.2). Retrieve from <http://epic.awi.de/41242/>.
- Hutchings, J. K., & Rigor, I. G. (2012). Role of ice dynamics in anomalous ice conditions in the Beaufort Sea during 2006 and 2007. *Journal of Geophysical Research*, *117*, C00E04. <https://doi.org/10.1029/2011JC007182>
- King, J., Skourup, H., Hvidegaard, S. M., Rösel, A., Gerland, S., Spreen, G., et al. (2018). Comparison of freeboard retrieval and ICE thickness calculation from ALS, ASIRAS, and CryoSat-2 in the Norwegian Arctic, to field measurements made during the N-ICE2015 expedition. *Journal of Geophysical Research: Oceans*, *123*, 1123–1141. <https://doi.org/10.1002/2017JC013233>
- Krishfield, R. A., Proshutinsky, A., Tateyama, K., Williams, W. J., Carmack, E. C., McLaughlin, F. A., & Timmermans, M.-L. (2014). Deterioration of perennial sea ice in the Beaufort Gyre from 2003 to 2012 and its impact on the oceanic freshwater cycle. *Journal of Geophysical Research, Oceans*, *119*, 1271–1305. <https://doi.org/10.1002/2013JC008999>
- Kurtz, J. C., & Harbeck, J. (2017). CryoSat-2 Level 4 Sea Ice Elevation, Freeboard, and Thickness, Version 1. Boulder, Colorado USA: NASA DAAC at the National Snow and Ice Data Center. <https://doi.org/10.5067/96J00KIFDASS>
- Kurtz, N. T., Galin, N., & Studinger, M. (2014). An improved CryoSat-2 sea ice freeboard retrieval algorithm through the use of waveform fitting. *The Cryosphere*, *8*(4), 1217–1237. <https://doi.org/10.5194/tc-8-1217-2014>
- Kurtz, N. T., & Markus, T. (2012). Satellite observations of Antarctic Sea ice thickness and volume. *Journal of Geophysical Research*, *117*, C08025. <https://doi.org/10.1029/2012JC008141>
- Kurtz, N. T., Markus, T., Cavalieri, D. J., Sparling, L. C., Krabill, W. B., Gasiewski, A. J., & Sonntag, J. G. (2009). Estimation of sea ice thickness distributions through the combination of snow depth and satellite laser altimetry data. *Journal of Geophysical Research*, *114*, C10007. <https://doi.org/10.1029/2009JC005292>
- Kurtz, N. T., Markus, T., Farrell, S. L., Worthen, D. L., & Boisvert, L. N. (2011). Observations of recent Arctic sea ice volume loss and its impact on ocean-atmosphere energy exchange and ice production. *Journal of Geophysical Research*, *116*, C04015. <https://doi.org/10.1029/2010JC006235>
- Kwok, R. (2015). Sea ice convergence along the Arctic coasts of Greenland and the Canadian Arctic Archipelago: Variability and extremes (1992–2014). *Geophysical Research Letters*, *42*, 7598–7605. <https://doi.org/10.1002/2015GL065462>
- Kwok, R., Cunningham, G., Hancock, D., Ivanoff, A., & Wimert, J. (2019). Ice, Cloud, and Land Elevation Satellite-2 Project: Algorithm Theoretical Basis Document (ATBD) for sea ice products. [https://icesat-2.gsfc.nasa.gov/science/data\\_products](https://icesat-2.gsfc.nasa.gov/science/data_products)
- Kwok, R., Cunningham, G., Markus, T., Hancock, D., Morison, J. H., Palm, S. P., et al. (2019a). ATLAS/ICESat-2 L3A sea ice heights, Version 1. Boulder, Colorado USA. NSIDC: National Snow and Ice Data Center. <https://doi.org/10.5067/ATLAS/ATL07.001>
- Kwok, R., Cunningham, G., Markus, T., Hancock, D., Morison, J. H., Palm, S. P., et al. (2019b). ATLAS/ICESat-2 L3A sea ice freeboard, Version 1. Boulder, Colorado USA. NSIDC: National Snow and Ice Data Center. <https://doi.org/10.5067/ATLAS/ATL10.001>
- Kwok, R., & Cunningham, G. F. (2008). ICESat over Arctic sea ice: Estimation of snow depth and ice thickness. *Journal of Geophysical Research*, *113*, C08010. <https://doi.org/10.1029/2008JC004753>
- Kwok, R., & Cunningham, G. F. (2015). Variability of Arctic sea ice thickness and volume from CryoSat-2. *Philosophical Transactions of the Royal Society A*, *373*(2045). <https://doi.org/10.1098/rsta.2014.0157>
- Kwok, R., Cunningham, G. F., Wensnahan, M., Rigor, I., Zwally, H. J., & Yi, D. (2009). Thinning and volume loss of the Arctic Ocean sea ice cover: 2003–2008. *Journal of Geophysical Research*, *114*, C07005.

- Kwok, R., Cunningham, G. F., Zwally, H. J., & Yi, D. (2007). Ice, Cloud, and land Elevation Satellite (ICESat) over Arctic sea ice: Retrieval of freeboard. *Journal of Geophysical Research*, *112*, C12013. <https://doi.org/10.1029/2006JC003978>
- Kwok, R., & Kacimi, S. (2018). Three years of sea ice freeboard, snow depth, and ice thickness of the Weddell Sea from Operation IceBridge and CryoSat-2. *The Cryosphere*, *12*(8), 2789–2801. <https://doi.org/10.5194/tc-12-2789-2018>
- Kwok, R., Kurtz, N. T., Brucker, L., Ivanoff, A., Newman, T., Farrell, S. L., et al. (2017). Inter-comparison of snow depth retrievals over Arctic sea ice from radar data acquired by Operation IceBridge. *The Cryosphere Discuss*, *2017*, 1–37. <https://doi.org/10.5194/tc-2017-103>
- Kwok, R., & Maksym, T. (2014). Snow depth of the Weddell and Bellingshausen sea ice covers from IceBridge surveys in 2010 and 2011: An examination. *Journal of Geophysical Research: Oceans*, *119*, 4141–4167. <https://doi.org/10.1002/2014JC009943>
- Kwok, R., Markus, T., Kurtz, N. T., Petty, A. A., Neumann, T. A., Farrell, S. L., et al. (2019). Surface height and sea ice freeboard of the Arctic Ocean from ICESat-2: Characteristics and early results. *Journal of Geophysical Research: Oceans*, *124*, 6942–6959. <https://doi.org/10.1029/2019JC015486>
- Kwok, R., Spreen, G., & Pang, S. (2013). Arctic sea ice circulation and drift speed: Decadal trends and ocean currents. *Journal of Geophysical Research: Oceans*, *118*, 2408–2425. <https://doi.org/10.1002/jgrc.20191>
- Lavergne, T., Eastwood, S., Teffah, Z., Schyberg, H., & Breivik, L.-A. (2010). Sea ice motion from low-resolution satellite sensors: An alternative method and its validation in the Arctic. *Journal of Geophysical Research*, *115*, C10032. <https://doi.org/10.1029/2009JC005958>
- Lavergne, T., Sørensen, A. M., Kern, S., Tonboe, R., Notz, D., Aaboe, S., et al. (2019). Version 2 of the EUMETSAT OSI SAF and ESA CCI sea-ice concentration climate data records. *The Cryosphere*, *13*(1), 49–78. <https://doi.org/10.5194/tc-13-49-2019>
- Laxon, S. W., Giles, K. A., Ridout, A. L., Wingham, D. J., Willatt, R., Cullen, R., et al. (2013). CryoSat-2 estimates of Arctic sea ice thickness and volume. *Geophysical Research Letters*, *40*, 732–737. <https://doi.org/10.1002/grl.50193>
- Lindsay, R., Haas, C., Hendricks, S., Hunkele, P., Kurtz, N., Paden, J., et al. (2012). Seasonal forecasts of Arctic sea ice initialized with observations of ice thickness. *Geophysical Research Letters*, *39*, L21502. <https://doi.org/10.1029/2012GL053576>
- Markus, T., Neumann, T., Martino, A., Abdalati, W., Brunt, K., Csatho, B., et al. (2017). The Ice, Cloud, and land Elevation Satellite-2 (ICESat-2): Science requirements, concept, and implementation. *Remote Sensing of Environment*, *190*, 260–273. <https://doi.org/10.1016/j.rse.2016.12.029>
- Maslanik, J., Stroeve, J., Fowler, C., & Emery, W. (2011). Distribution and trends in Arctic sea ice age through spring 2011. *Geophysical Research Letters*, *38*, L13502. <https://doi.org/10.1029/2011GL047735>
- Maslanik, J., & Stroeve, J. C. (1999). Near-real-time DMSP SSMIS daily polar gridded sea ice concentrations, Version 1. [January 2016–December 2016]. Boulder, Colorado USA: NASA DAAC the National Snow and Ice Data Center. <https://doi.org/10.5067/U8C09DWVX9LM>
- Meier, W. N. (2005). Comparison of passive microwave ice concentration algorithm retrievals with AVHRR imagery in arctic peripheral seas. *IEEE Transactions on Geoscience and Remote Sensing*, *43*(6), 1324–1337. <https://doi.org/10.1109/TGRS.2005.846151>
- Meier, W. N., Fetterer, F., & Windnagel, A. K. (2017). Near-real-time NOAA/NSIDC Climate Data Record of passive microwave sea ice concentration, Version 1. <https://doi.org/10.7265/N5FF3QJ6>
- Nandan, V., Geldsetzer, T., Yackel, J., Mahmud, M., Scharien, R., Howell, S., et al. (2017). Effect of snow salinity on CryoSat-2 Arctic first-year sea ice freeboard measurements. *Geophysical Research Letters*, *44*, 10,419–10,426. <https://doi.org/10.1002/2017GL074506>
- National Research Council (2007). *Earth science and applications from space: National imperatives for the next decade and beyond*. Washington, DC: The National Academies Press. <https://doi.org/10.17226/11820>
- Neumann, T. A., Brenner, A., Hancock, D., Robbins, J., Luthke, S., Harbeck, K., & Lee, J. (2019a). ATLAS/ICESat-2 L2A Global Geolocated Photon Data, Version 1. Boulder, Colorado USA. NSIDC: National Snow and Ice Data Center. <https://doi.org/10.5067/ATLAS/ATL03.001>
- Neumann, T. A., Brenner, A., Hancock, D., Robbins, J., Saba, J., Harbeck, K., & Gibbons, A. (2019b). Ice, Cloud, and Land Elevation Satellite-2 Project: Algorithm Theoretical Basis Document (ATBD) for Global Geolocated Photons ATL03. [https://icesat-2.gsfc.nasa.gov/science/data\\_products](https://icesat-2.gsfc.nasa.gov/science/data_products)
- Neumann, T. A., Martino, A. J., Markus, T., Bae, S., Bock, M. R., Brenner, A. C., et al. (2019). The Ice, Cloud, and Land Elevation Satellite-2 mission: A global geolocated photon product derived from the Advanced Topographic Laser Altimeter System. *Remote Sensing of Environment*, *233*, 111325. <https://doi.org/10.1016/j.rse.2019.111325>
- Parkinson, C. L. (2019). A 40-y record reveals gradual Antarctic sea ice increases followed by decreases at rates far exceeding the rates seen in the Arctic. *Proceedings of the National Academy of Sciences*, *116*(29), 14414–14423. <https://doi.org/10.1073/pnas.1906556116>
- Parkinson, C. L., Cavalieri, D. J., Gloersen, P., Zwally, H. J., & Comiso, J. C. (1999). Arctic sea ice extents, areas, and trends, 1978–1996. *Journal of Geophysical Research*, *104*, 20,837–20,856. <https://doi.org/10.1029/1999JC900082>
- Petty, A. A., Holland, M. M., Bailey, D. A., & Kurtz, N. T. (2018). Warm Arctic, increased winter sea ice growth? *Geophysical Research Letters*, *45*, 12,922–12,930. <https://doi.org/10.1029/2018GL079223>
- Petty, A. A., Hutchings, J. K., Richter-Menge, J. A., & Tschudi, M. A. (2016). Sea ice circulation around the Beaufort Gyre: The changing role of wind forcing and the sea ice state. *Journal of Geophysical Research: Oceans*, *121*, 3278–3296. <https://doi.org/10.1002/2015JC010903>
- Petty, A. A., Markus, T., & Kurtz, N. T. (2017). Improving our understanding of Antarctic sea ice with NASA's Operation IceBridge and the upcoming ICESat-2 Mission, *15*(2).
- Petty, A. A., Stroeve, J. C., Holland, P. R., Boisvert, L. N., Bliss, A. C., Kimura, N., & Meier, W. N. (2018). The Arctic sea ice cover of 2016: A year of record-low highs and higher-than-expected lows. *The Cryosphere*, *12*(2), 433–452. <https://doi.org/10.5194/tc-12-433-2018>
- Petty, A. A., Tsamados, M. C., Kurtz, N. T., Farrell, S. L., Newman, T., Harbeck, J. P., et al. (2016). Characterizing Arctic sea ice topography using high-resolution IceBridge data. *The Cryosphere*, *10*(3), 1161–1179. <https://doi.org/10.5194/tc-10-1161-2016>
- Petty, A. A., Webster, M., Boisvert, L., & Markus, T. (2018). The NASA Eulerian snow on sea ice model (NESOSIM) v1.0: Initial model development and analysis. *Geoscientific Model Development*, *11*(11), 4577–4602. <https://doi.org/10.5194/gmd-11-4577-2018>
- Ricker, R., Hendricks, S., Helm, V., Skourup, H., & Davidson, M. (2014). Sensitivity of CryoSat-2 Arctic sea ice freeboard and thickness on radar-waveform interpretation. *The Cryosphere*, *8*(4), 1607–1622. <https://doi.org/10.5194/tc-8-1607-2014>
- Ricker, R., Hendricks, S., Kaleschke, L., Tian-Kunze, X., King, J., & Haas, C. (2017). A weekly Arctic sea-ice thickness data record from merged CryoSat-2 and SMOS satellite data. *The Cryosphere*, *11*(4), 1607–1623. <https://doi.org/10.5194/tc-11-1607-2017>
- Schröder, D., Feltham, D. L., Tsamados, M., Ridout, A., & Tilling, R. (2019). New insight from CryoSat-2 sea ice thickness for sea ice modelling. *The Cryosphere*, *13*(1), 125–139. <https://doi.org/10.5194/tc-13-125-2019>
- Screen, J. A., & Francis, J. A. (2016). Contribution of sea-ice loss to Arctic amplification is regulated by Pacific Ocean decadal variability. *Nature Climate Change*, *6*(9), 856–860. <https://doi.org/10.1038/nclimate3011>

- Serreze, M. C., Barrett, A. P., Slater, A. G., Woodgate, R. A., Aagaard, K., Lammers, R. B., et al. (2006). The large-scale freshwater cycle of the Arctic. *Journal of Geophysical Research*, *111*, C11010. <https://doi.org/10.1029/2005JC003424>
- Stroeve, J., & Notz, D. (2018). Changing state of Arctic sea ice across all seasons. *Environmental Research Letters*, *13*(10), 103,001. <https://doi.org/10.1088/1748-9326/aade56>
- Stroeve, J., Serreze, M., Drobot, S., Gearheard, S., Holland, M., Maslanik, J., et al. (2008). Arctic sea ice extent plummets in 2007. *Eos, Transactions American Geophysical Union*, *89*(2), 13–14. <https://doi.org/10.1029/2008EO020001>
- Thomas, D. N., & Dieckmann, G. S. (2009). *Sea ice*, (2nd ed.). Hoboken, N. J: Wiley-Blackwell.
- Tilling, R. L., Ridout, A., & Shepherd, A. (2018). Estimating Arctic sea ice thickness and volume using CryoSat-2 radar altimeter data. *Advances in Space Research*, *62*(6), 1203–1225. <https://doi.org/10.1016/j.asr.2017.10.051>
- Timco, G. W., & Frederking, R. M. W. (1996). A review of sea ice density. *Cold Regions Science and Technology*, *24*(1), 1–6. [https://doi.org/10.1016/0165-232X\(95\)00007-X](https://doi.org/10.1016/0165-232X(95)00007-X)
- Vancoppenolle, M., Meiners, K. M., Michel, C., Bopp, L., Brabant, F., Carnat, G., et al. (2013). Role of sea ice in global biogeochemical cycles: Emerging views and challenges. *Quaternary Science Reviews*, *79*, 207–230. <https://doi.org/10.1016/j.quascirev.2013.04.011>
- Wang, C., Graham, R. M., Wang, K., Gerland, S., & Granskog, M. A. (2019). Comparison of ERA5 and ERA-Interim near-surface air temperature, snowfall and precipitation over Arctic sea ice: Effects on sea ice thermodynamics and evolution. *The Cryosphere*, *13*(6), 1661–1679. <https://doi.org/10.5194/tc-13-1661-2019>
- Warren, S. G., Rigor, I. G., Untersteiner, N., Radionov, V. F., Bryazgin, N. N., Aleksandrov, Y. I., & Colony, R. (1999). Snow depth on Arctic sea ice. *Journal of Climate*, *12*(6), 1814–1829. [https://doi.org/10.1175/1520-0442\(1999\)012<1814:SDOASI>2.0.CO;2](https://doi.org/10.1175/1520-0442(1999)012<1814:SDOASI>2.0.CO;2)
- Webster, M. A., Rigor, I. G., Nghiem, S. V., Kurtz, N. T., Farrell, S. L., Perovich, D. K., & Sturm, M. (2014). Interdecadal changes in snow depth on Arctic sea ice. *Journal of Geophysical Research: Oceans*, *119*, 5395–5406. <https://doi.org/10.1002/2014JC009985>
- Willatt, R., Laxon, S., Giles, K., Cullen, R., Haas, C., & Helm, V. (2011). Ku-band radar penetration into snow cover on Arctic sea ice using airborne data. *Annals of Glaciology*, *52*(57), 197–205. <https://doi.org/10.3189/172756411795931589>
- Wingham, D. J., Francis, C. R., Baker, S., Bouzinac, C., Brockley, D., Cullen, R., et al. (2006). CryoSat: A mission to determine the fluctuations in Earth's land and marine ice fields. *Advances in Space Research*, *37*(4), 841–871. <https://doi.org/10.1016/j.asr.2005.07.027>
- Zwally, H. J., Yi, D., Kwok, R., & Zhao, Y. (2008). ICESat measurements of sea ice freeboard and estimates of sea ice thickness in the Weddell Sea. *Journal of Geophysical Research*, *113*, C02S15. <https://doi.org/10.1029/2007JC004284>
- Zwally, H. J., Schutz, B., Abdalati, W., Abshire, J., Bentley, C., Brenner, A., et al. (2002). ICESat's laser measurements of polar ice, atmosphere, ocean, and land. *Journal of Geodynamics*, *34*(3–4), 405–445. [https://doi.org/10.1016/S0264-3707\(02\)00042-X](https://doi.org/10.1016/S0264-3707(02)00042-X)